

GALEX ULTRAVIOLET IMAGING OF DWARF GALAXIES AND STAR FORMATION RATES*

DEIDRE A. HUNTER¹, BRUCE G. ELMEGREEN², AND BONNIE C. LUDKA^{1,3}

¹ Lowell Observatory, 1400 West Mars Hill Road, Flagstaff, AZ 86001, USA; dah@lowell.edu, ludkabc@gmail.com

² IBM T. J. Watson Research Center, P.O. Box 218, Yorktown Heights, NY 10598, USA; bge@watson.ibm.com

Received 2009 June 04; accepted 2009 November 17; published 2010 January 8

ABSTRACT

We present ultraviolet-integrated and azimuthally averaged surface photometric properties of a sample of 44 dwarf irregular (dIm), blue compact dwarf, and Sm galaxies measured from archival near-ultraviolet (NUV) and far-ultraviolet (FUV) images obtained with the *Galaxy Evolution Explorer* (GALEX). We compare the UV to H α and V-band properties and convert FUV, H α , and V-band luminosities into star formation rates (SFRs). We also model the star formation history from colors and compare the integrated SFRs and SFR profiles with radius for these methods. In most galaxies, the UV photometry extends beyond H α in radius, providing a better measure of the star formation activity in the outer disks. The H α appears to be lacking in the outer disk because of faintness in low-density gas. The FUV and V-band profiles are continuous with radius, although they sometimes have a kink from a double exponential disk. There is no obvious difference in star formation properties between the inner and outer disks. No disk edges have been observed, even to stellar surface densities as low as $0.1 M_{\odot} \text{ pc}^{-2}$ and SFRs as low as $10^{-4} M_{\odot} \text{ yr}^{-1} \text{ kpc}^{-2}$. Galaxies with low H I to luminosity ratios have relatively low FUV compared to V-band emission in the outer parts, suggesting a cessation of star formation there. Galaxies with relatively high H I apparently have fluctuating star formation with a gigayear timescale.

Key words: galaxies: dwarf – galaxies: photometry

Online-only material: color figures

1. INTRODUCTION

Outer edges of dwarf irregular (dIm) galaxies present an extreme environment for star formation. Dwarf galaxies already challenge models of star formation because of their low gas densities even in the central regions (Hunter & Plummer 1996; Meurer et al. 1996; van Zee et al. 1997; Hunter et al. 1998; Rafikov 2001). Outer parts of dwarfs, where the gas density is even lower, therefore, present a particularly difficult test of our understanding of the cloud/star formation process. Yet, from broadband images we see that stars have formed in the outer parts to very low surface brightness levels (for example, D. Hunter et al. 2010, in preparation).

We are using UV images obtained with the *Galaxy Evolution Explorer* satellite (GALEX; Martin et al. 2005) to trace and characterize star formation from the centers out into the outer disks of dwarf galaxies where H α may not be an effective tracer of recent star formation (see, for example, Thilker et al. 2005, 2007a; Boissier et al. 2007). Fortunately, the UV—ultraviolet light coming directly from OB stars—can easily trace young stars in the outer galaxy, and the UV has the advantage in a patchy star-forming environment of integrating over a longer timescale (≤ 100 – 200 Myr) than does H α (≤ 10 Myr).

In this paper, we compare the UV surface brightness profiles to those of H α and to those of the older stars as seen in broadband images. We compute integrated and azimuthally averaged profiles of several measures of star formation rates (SFRs): derived from far-ultraviolet (FUV), H α , and V-band luminosities and model stellar population fits to broadband UV, optical, and near-infrared colors. In a companion paper,

we examine characteristics of individual star-forming regions identified on the GALEX images and compare those in the outer disk with those in the inner disk (Melena et al. 2009). The galaxies discussed in these two studies are also part of a larger, multi-wavelength survey of dIm, blue compact dwarf (BCD), and Sm galaxies that has been assembled in order to examine the drivers of star formation in tiny galaxies (Hunter & Elmegreen 2004, 2006).

2. THE DATA

The galaxies in this investigation are a sub-sample of a large multi-wavelength survey of 136 relatively normal nearby galaxies without spiral arms (94 dIm, 24 BCDs, and 18 Sm galaxies; Hunter & Elmegreen 2004, 2006). That survey is representative of the range in galactic parameters exhibited by dwarfs, and is aimed at understanding star formation processes in dwarf galaxies. The *UBV JHK* and H α data obtained as part of that survey are described by Hunter & Elmegreen.

To extend this survey into the UV, we obtained images from the GALEX archives for 44 of our 136 dwarf galaxies, including 29 dIm, 8 BCDs, and 7 Sm galaxies. The galaxies are listed in Table 1 along with the exposure times and tile name of the GALEX images. GALEX images simultaneously in two channels: FUV with a bandpass of 1350–1750 Å, an effective wavelength of 1516 Å, and a resolution of $4''.0$ and near-ultraviolet (NUV) with a bandpass of 1750–2800 Å, an effective wavelength of 2267 Å, and a resolution of $5''.6$. The images were processed through the GALEX pipeline and were retrieved as final intensity maps with a $1''.5$ pixel scale. The GALEX field of view is a circle with $1''.2$ diameter, and we have extracted a portion around our target galaxies. Figure 1 shows V, H α , and UV images of IC 1613 as an example of the data. The H α and V-band images are described by Hunter & Elmegreen (2004, 2006). In Table 2, we collect integrated

* Based on observations made with the NASA *Galaxy Evolution Explorer* (GALEX). GALEX is operated for NASA by the California Institute of Technology under NASA contract NAS5-98034.

³ Current address: Scripps Institution of Oceanography, University of California, San Diego, CA 92121 USA.

Table 1
Galaxy Sample and *GALEX* Observations

Galaxy	Other Names	D^a (Mpc)	$E(B - V)_f^b$	FUV Exp (s)	NUV Exp (s)	Tile Name
Im galaxies						
DDO 50	PGC 23324, UGC 4305, Holmberg II, VIIZw223	3.4	0.02	1674	1521	NGA_HolmbergII
DDO 52	PGC 23769, UGC 4426	6.0	0.03	1678	1522	GI1_047032_UGC04426_0001
DDO 53	PGC 24050, UGC 4459, VIIZw238	3.6	0.03	1672	1502	NGA_DDO053
DDO 63	PGC 27605, Holmberg I, UGC 5139	3.8	0.01	1676	1544	NGA_HolmbergI
DDO 68	PGC 28714, UGC 5340	7.0	0.01	1435	1305	GI1_047036_UGC05340
DDO 70	PGC 28913, UGC 5373, Sextans B	1.3	0.01	1076	966	NGA_SextansB
DDO 75	PGC 29653, UGCA 205, Sextans A	1.3	0.02	1663	1512	NGA_SextansA
DDO 99	PGC 37050, UGC 6817	4.1	0.00	2348	2196	GI1_047053_UGC06817
DDO 101	PGC 37449, UGC 6900	9.0	0.01	1668	1563	GI1_047054_UGC06900_0001
DDO 115	PGC 39142, UGC 7254, IC 3059	3.2	0.00	1651	2381	VIRGO_SPEC_1
DDO 120	PGC 39918, UGC 7408	8.0	0.00	1504	2544	GI1_047066_NGC4288
DDO 126	PGC 40791, UGC 7559	4.9	0.00	1675	1563	GI1_047068_UGC07559
DDO 143	PGC 42901, UGC 7916, IZw042	9.8	0.00	1673	1569	GI1_047081_UGC07916
DDO 154	PGC 43869, UGC 8024, NGC 4789A	4.3	0.01	1432	1312	NGA_DDO154
DDO 167	PGC 45939, UGC 8308	4.2	0.00	1564	2856	GI1_047088_UGC08308
DDO 168	PGC 46039, UGC 8320	3.5	0.00	1564	2856	GI1_047088_UGC08308
DDO 183	PGC 49158, UGC 8760	5.1	0.00	2390	2231	GI1_047098_UGC08760
DDO 210	PGC 065367, Aquarius dwarf	0.9	0.04	1669	1472	GI1_047107_DDO210
DDO 215	PGC 69415, UGCA 433	14.7	0.03	1233	40	GI1_009029_UGCA433
DDO 216	PGC 71538, UGC 12613, Peg DIG	0.9	0.02	1557	2665	MISDR2_28664_0746
F565-V2	LEDA 086670	55.0	0.02	1668	1515	NGA_LSBC_F565
IC 1613	PGC 3844, UGC 668, DDO 8	0.7	0.00	1676	1494	NGA_IC16134
LGS3	PGC 3792, Pisces dwarf	0.6	0.04	1673	1487	NGA_LGS3
M81dwA	PGC 23521	3.6	0.02	1674	1521	NGA_HolmbergII
NGC 1156	PGC 11329, UGC 2455	7.8	0.17	1495	1270	NGA_NGC1156
NGC 1569	PGC 15345, UGC 3056, Arp 210, VIIZw16	2.5	0.51	6988	6101	NGA_NGC1569
NGC 2366	PGC 21102, UGC 3851, DDO 42	3.2	0.04	2889	2617	NGA_NGC2366
NGC 6822	PGC 63616, IC 4895, DDO 209, Barnard's Galaxy	0.5	0.21	4483	5132	NGA_NGC6822
WLM	PGC 143, UGCA 444, DDO 221	1.0	0.02	1423	1294	NGA_WLM
BCD galaxies						
Haro 3	PGC 32103, UGC 5860, NGC 3353, Mrk 35	15.5	0.00	12618	30378	LOCK_10
Haro 20	PGC 12922, UGCA 073	27.6	0.03	3319	3066	MISWZS03_27657_0283
Haro 23	PGC 29347, UGCA 201	20.2	0.01	1594	1452	GI1_047038_UGC05427
Haro 29	PGC 40665, UGCA 281, Mrk 209, IZw36	5.4	0.00	1657	1548	GI1_047067_UGCA281
Haro 36	PGC 43124, UGC 7950	9.0	0.00	1648	1531	GI1_047082_UGC07950
Mrk 757	PGC 38277	8.9	0.01	1677	1559	GI1_047057_Mrk0757
NGC 6789	PGC 063000, UGC 11525	3.6	0.08	1360	1164	NGA_NGC6789
VIIZw403	PGC 35286, UGC 6456, A1124 + 79	4.4	0.02	1617	1479	NGA_VIIZw403
Sm galaxies						
DDO 88	PGC 32226, UGC 5889, NGC 3377A	7.4	0.01	0	1647	NGA_NGC3377
DDO 150	PGC 43255, UGC 7971, NGC 4707, IZw43	8.5	0.00	1648	1531	GI1_047082_UGC07950
DDO 180	PGC 48179	18.8	0.03	0	4388	GI1_024002_DEEP_IMPACT
F583-1	LSBC D584-04	37.0	0.03	1551	2386	GI1_073008_J155912p204531
NGC 2552	PGC 23340, UGC 4325	8.5	0.04	1677	3066	MISDR1_03473_0440
NGC 3109	PGC 29128, UGCA 194, DDO 236	1.3	0.04	6043	5177	NGA_NGC3109
NGC 3510	PGC 33408, UGC 6126, Haro 26	10.4	0.00	1547	1441	GI1_047049_NGC3510

Notes.

^a See references in Hunter & Elmegreen (2006).

^b Foreground reddening from Burstein & Heiles (1984).

optical *UBV*, near-IR *JHK*, and $H\alpha$ photometry of our sample from Hunter & Elmegreen.

We subtracted or masked foreground stars and background galaxies, and removed sky from the *GALEX* NUV and FUV images. In some cases, the sky was a constant determined from regions around the galaxy, but in other cases the sky was determined from a low-order, two-dimensional fit to the surroundings. We geometrically transformed the UV images to match the orientation and scale of our $H\alpha$ and *V*-band images. We measured surface photometry in the NUV and FUV images in fixed ellipses of increasing semimajor axis length, using

the center, position angle, ellipticity, and step size that were used to do surface photometry on the optical images (Hunter & Elmegreen 2006).

We corrected the UV photometry for extinction using the same total reddening $E(B - V)_t$ as was used for correcting the *V*-band photometry in the larger survey: foreground $E(B - V)_f$ from Burstein & Heiles (1984) given in Table 1 plus 0.05 mag for internal reddening of the stars. The $H\alpha$ photometry was corrected with 0.1 mag for the internal reddening in H II regions. This level of internal reddening is consistent with measurements of the Balmer decrement in H II regions in a sample of 39 dIm

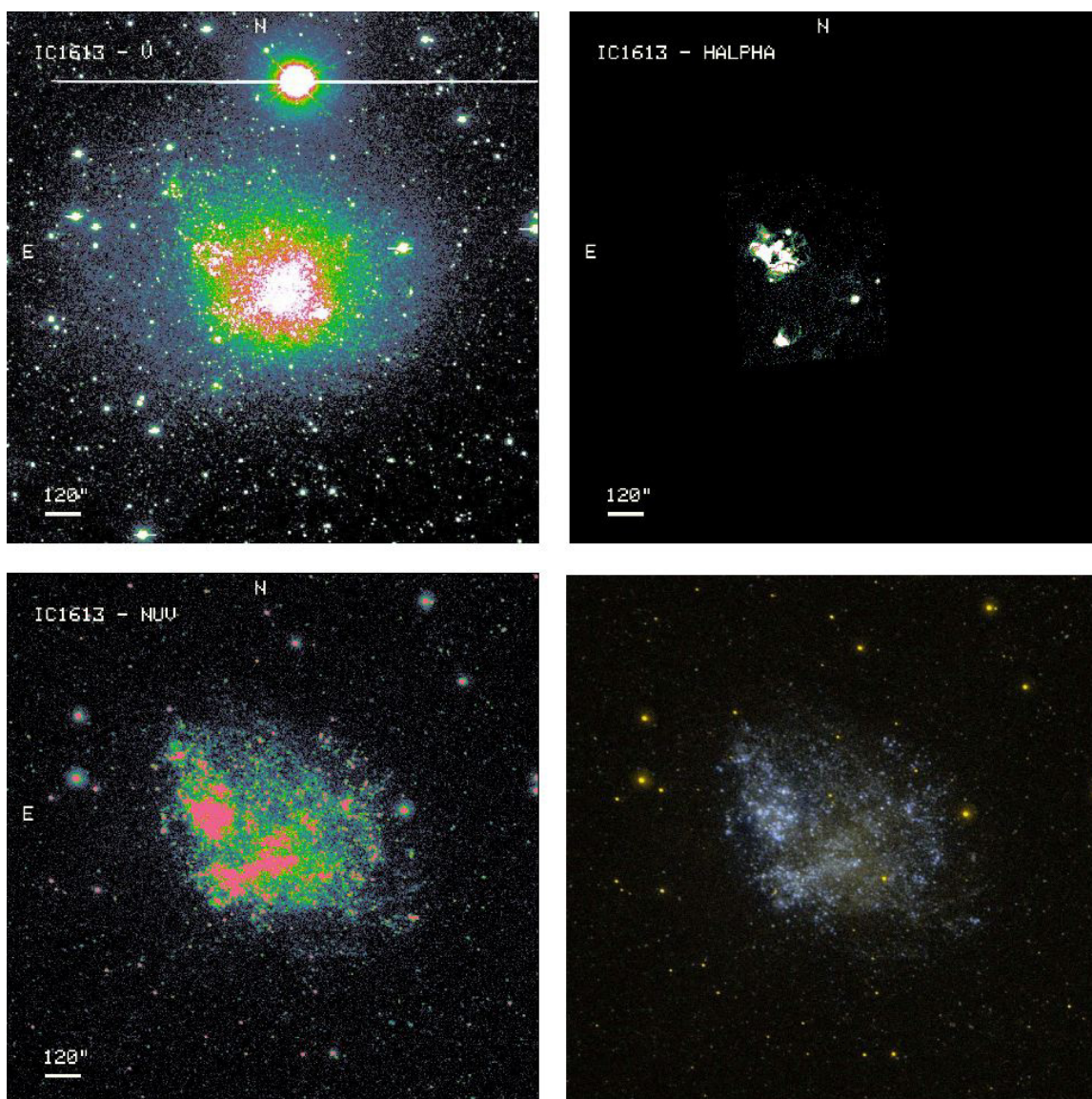


Figure 1. Images of IC 1613 as an example of the data. V, H α , and GALEX NUV images are shown in false color and with the same field of view and pixel scale. The image in the lower right is from the GALEX pipeline and is a combination of the FUV and NUV images. It has nearly the same field of view as the other images. The V and H α images are from Hunter & Elmegreen (2004, 2006).

galaxies (Hunter & Hoffman 1999). There the average reddening in H II regions is 0.1, and we have taken half of this to represent the stars outside of H II regions.

We combined the $E(B - V)_r$ with the extinction law of Cardelli et al. (1989) to produce the extinction $A_{\text{FUV}} = 8.24E(B - V)_r$, and, interpolating over the 2175 Å bump, $A_{\text{NUV}} = 7.39E(B - V)_r$. However, the FUV extinction law varies from galaxy to galaxy, and the NUV filter straddles the 2175 Å extinction feature, which also varies not only from galaxy to galaxy but also from place to place within galaxies (for example, Gordon et al. 2003). Star formation activity appears to play as important a role, perhaps even more important, than metallicity in determining the UV extinction curve and the strength of the 2175 Å bump. In the metal-poor Small Magellanic Cloud (SMC), for example, Gordon & Clayton (1998) have shown that lines of sight through the actively star-forming bar have UV extinction curves that are linear with $1/\lambda$, rising more steeply into the FUV than in the Milky Way, and

no 2175 Å bump is present, while a sight line through the quiescent wing has an extinction curve that is similar to that in the Milky Way with a shallower slope into the FUV and a 2175 Å bump. Similarly in the Large Magellanic Cloud (LMC), regions of intense star formation have stronger extinction into the FUV and weaker 2175 Å than the average LMC extinction curve (see, for example, Gordon et al. 2003). Furthermore, the reddening parameter $R_V = A_V/E(B - V)$ varies by 25% within the LMC, for example. In our dwarf galaxies, the level of star formation activity is highly variable from galaxy to galaxy and from place to place within a galaxy. To complicate things further, the reddening we need to correct is the result of two different reddening laws: that due to the Milky Way and that due to the dwarf galaxy under study. Wyder et al. (2007) have dealt with this for a large sample of galaxies by adopting the Cardelli et al. extinction law for the Milky Way and determining the best average reddening from convolving theoretical galaxy spectral energy distributions (SEDs) with the

Table 2
Integrated Optical and Infrared Photometry^a

Galaxy	M_V	σ_{M_V}	$(U-B)_0$	σ_{U-B}	$(B-V)_0$	σ_{B-V}	$(J-H)_0$	σ_{J-H}	$(H-K)_0$	σ_{H-K}	$\log L_{H\alpha}$ (erg s ⁻¹)	$\sigma_{\log L_{H\alpha}}$ (erg s ⁻¹)
Im galaxies												
DDO 50	-16.61	0.00	-0.41	0.00	0.22	0.00	40.025	0.001
DDO 52	-14.27	0.03	-0.02	0.10	0.39	0.04	38.213	0.013
DDO 53	-13.84	0.01	-0.53	0.01	0.41	0.01	0.45	2.17	38.947	0.001
DDO 63	-14.73	0.02	-0.18	0.05	0.20	0.02	38.977	0.010
DDO 68	-15.17	0.02	-0.24	0.05	0.12	0.03	38.457	0.040
DDO 70	-14.10	0.00	-0.11	0.00	0.36	0.00	38.171	0.003
DDO 75	-13.91	0.01	-0.54	0.02	0.19	0.01	39.060	0.001
DDO 99	-14.88	0.01	-0.20	0.03	0.28	0.02	38.931	0.006
DDO 101	-15.75	0.01	-0.01	0.02	0.61	0.02	38.921	0.008
DDO 115	-13.28	0.01	-0.08	0.02	0.52	0.02	38.118	0.005
DDO 120	-16.33	0.01	-0.11	0.03	0.35	0.01	0.000	0.000
DDO 126	-14.85	0.01	-0.35	0.03	0.29	0.02	39.166	0.004
DDO 143	-15.58	0.02	-0.73	0.02	0.35	0.02	39.480	0.011
DDO 154	-14.51	0.01	-0.32	0.05	0.30	0.03	38.835	0.005
DDO 167	-12.98	0.04	-0.38	0.06	0.19	0.05	38.329	0.005
DDO 168	-15.27	0.00	-0.25	0.01	0.37	0.01	0.32	0.12	0.66	0.20	39.026	0.002
DDO 183	-14.54	0.01	-0.20	0.05	0.31	0.02	38.352	0.016
DDO 210	-10.88	0.01	-0.09	0.03	0.50	0.01	0.000	0.000
DDO 215	-15.63	0.06	-0.40	0.06	0.10	0.06	39.123	0.024
DDO 216	-13.29	0.00	-0.03	0.00	0.66	0.00	36.853	0.026
F565-V2	-17.65	0.04	38.195	0.090
IC 1613	-14.60	0.00	0.13	0.01	0.43	0.01	38.628	0.000
LGS3	-9.41	0.03	0.07	0.07	0.63	0.05	0.000	0.000
M81dwA	-11.73	0.06	-0.33	0.16	0.27	0.08	0.000	0.000
NGC 1156	-18.67	0.00	-0.27	0.01	0.38	0.00	0.54	0.01	0.25	0.02	40.680	0.001
NGC 1569	-17.57	0.00	-0.57	0.00	0.25	0.00	0.58	0.01	0.13	0.02	40.754	0.000
NGC 2366	-16.66	0.00	-0.39	0.00	0.30	0.00	0.37	0.05	0.14	0.15	40.202	0.000
NGC 6822	-15.22	0.00	-0.34	0.00	0.46	0.00	39.110	0.001
WLM	-14.39	0.00	0.17	0.01	0.41	0.00	38.410	0.001
BCD galaxies												
Haro 3	-18.23	0.02	-0.43	0.01	0.40	0.03	0.63	0.05	40.899	0.000
Haro 20	-18.32	0.01	0.08	0.03	0.34	0.02	40.180	0.002
Haro 23	-17.72	0.00	-0.22	0.01	0.47	0.01	0.88	0.13	40.218	0.001
Haro 29	-14.47	0.00	-0.50	0.01	0.26	0.01	0.53	0.20	39.763	0.001
Haro 36	-15.84	0.00	-0.04	0.01	0.39	0.01	39.446	0.003
Mrk 757	-15.46	0.01	-0.26	0.05	0.45	0.02	39.231	0.002
NGC 6789	-14.77	0.00	-0.14	0.01	0.52	0.00	38.604	0.007
VIIZw403	-14.27	0.01	-0.49	0.01	0.28	0.01	39.353	0.001
Sm galaxies												
DDO 88	-15.87	0.01	-0.08	0.02	0.53	0.02	38.886	0.013
DDO 150	-16.31	0.01	-0.25	0.04	0.31	0.02	39.671	0.003
DDO 180	-19.19	0.00	-0.17	0.02	0.48	0.01	0.71	0.03	40.678	0.002
F583-1	-17.17	0.02	-0.37	0.06	0.28	0.03	39.969	0.010
NGC 2552	-17.34	0.00	-0.22	0.01	0.25	0.01	0.52	0.06	0.25	0.08	40.055	0.002
NGC 3109	-17.90	0.00	-0.17	0.00	0.43	0.00	39.520	0.000
NGC 3510	-17.27	0.00	-0.31	0.01	0.34	0.01	0.63	0.04	0.27	0.09	40.452	0.002

Note. ^a From Hunter & Elmegreen (2004, 2006).

GALEX filter transmission curves. In the same manner, we have examined the results of convolving different SMC, LMC, and Milky Way extinction curves (Cardelli et al. 1989; Gordon et al. 2003) with constant SFR galaxy SEDs constructed from the Bruzual & Charlot (2003) stellar population library and with the *GALEX* filter transmission curves. The $A_\lambda/E(B-V)$ vary by 1.5 mag depending on the extinction curve. Considering the variety of environments represented by our sample and the fact that extinction is minimal except for a few galaxies with higher than average foreground extinction, we decided to adopt the Wyder et al. extinctions: $A_{FUV} = 8.24E(B-V)_r$ and

$A_{NUV} = 8.2E(B-V)_r$. For most of our galaxies, the variations represented by alternate extinction laws result in differences of order 0.05 mag.

We used a single extinction correction for all radii within each galaxy. This is justified by the lack of metallicity gradients in dwarfs and the correlation between metallicity and attenuation seen in spirals (Boissier et al. 2007). On the other hand, nothing is known about the outer disks of dwarfs, beyond where $H\alpha$ emission is no longer detected, and there is some evidence for large quantities of cold dust out there (Galliano et al. 2003). However, Boissier et al., based on *IRAS* observations, suggest

Table 3
Integrated *GALEX* Photometry

Galaxy	M_{NUV}^a	$\sigma_{M_{\text{NUV}}}$	$(\text{FUV} - \text{NUV})_0$	$\sigma_{\text{FUV}-\text{NUV}}$	$(\text{NUV} - V)_0^a$	$\sigma_{\text{NUV}-V}$	$\log L_{\text{H}\alpha}/L_{\text{NUV}}^b$	$\log L_{\text{NUV}}^c$	$\sigma_{\log L_{\text{NUV}}}$
Im galaxies									
DDO 50	-15.77	0.00	0.08	0.00	0.88	0.00	-1.59	26.98	0.00
DDO 52	-12.65	0.01	0.47	0.02	1.62	0.04	-2.17	25.73	0.00
DDO 53	-12.76	0.01	0.15	0.02	1.08	0.01	-1.48	25.80	0.00
DDO 63	-13.44	0.00	0.23	0.01	1.29	0.02	-1.72	26.04	0.00
DDO 68	-14.43	0.00	0.14	0.01	0.74	0.02	-2.64	26.44	0.00
DDO 70	-12.41	0.00	0.38	0.01	1.69	0.00	-2.12	25.63	0.00
DDO 75	-13.26	0.00	0.21	0.00	0.66	0.01	-1.57	25.97	0.00
DDO 99	-13.62	0.00	0.34	0.01	1.26	0.01	-1.84	26.12	0.00
DDO 101	-13.15	0.01	0.64	0.03	2.60	0.02	-1.66	25.93	0.00
DDO 115	-11.22	0.01	0.43	0.02	2.06	0.02	-1.70	25.16	0.00
DDO 120	-14.27	0.00	0.57	0.01	2.06	0.01	...	26.38	0.00
DDO 126	-13.68	0.00	0.27	0.01	1.18	0.01	-1.63	26.14	0.00
DDO 143	-14.56	0.00	0.18	0.01	1.02	0.02	-1.67	26.49	0.00
DDO 154	-13.70	0.00	0.03	0.01	0.81	0.02	-1.97	26.15	0.00
DDO 167	-12.16	0.00	0.24	0.01	0.81	0.04	-1.86	25.53	0.00
DDO 168	-13.81	0.00	0.29	0.00	1.46	0.00	-1.82	26.19	0.00
DDO 183	-13.18	0.00	0.20	0.01	1.37	0.02	-2.24	25.94	0.00
DDO 210	-8.77	0.05	0.38	0.09	2.11	0.05	...	24.20	0.04
DDO 215	-14.75	0.01	0.09	0.10	0.88	0.07	-2.10	26.57	0.00
DDO 216	-9.96	0.00	1.00	0.02	3.33	0.01	-2.45	24.66	0.00
F565-V2	-14.63	0.04	0.33	0.07	3.02	0.06	-2.98	26.55	0.02
IC 1613	-13.20	0.00	0.20	0.00	1.41	0.00	-1.97	25.95	0.00
LGS3	-6.68	0.04	1.32	0.16	2.73	0.05	...	23.34	0.02
M81dwA	-10.94	0.01	0.13	0.02	0.79	0.06	...	25.04	0.00
NGC 1156	-17.03	0.00	0.43	0.01	1.64	0.00	-1.46	27.48	0.00
NGC 1569	-16.74	0.00	0.75	0.00	0.83	0.00	-1.27	27.36	0.00
NGC 2366	-15.65	0.00	0.22	0.00	1.01	0.00	-1.38	26.93	0.00
NGC 6822	-14.12	0.00	0.38	0.00	1.10	0.00	-1.86	26.12	0.00
WLM	-12.96	0.00	0.31	0.00	1.42	0.00	-2.10	25.85	0.00
BCD galaxies									
Haro 3	-16.89	0.00	0.31	0.00	1.34	0.02	-1.18	27.42	0.00
Haro 20	-16.28	0.00	0.43	0.01	2.05	0.02	-1.65	27.18	0.00
Haro 23	-16.26	0.00	0.49	0.01	1.46	0.01	-1.61	27.17	0.00
Haro 29	-13.81	0.00	0.08	0.01	0.66	0.01	-1.08	26.19	0.00
Haro 36	-15.10	0.00	0.46	0.01	0.74	0.00	-1.92	26.71	0.00
Mrk 757	-13.86	0.00	0.23	0.01	1.60	0.01	-1.63	26.21	0.00
NGC 6789	-12.65	0.02	0.62	0.05	2.12	0.02	-1.78	25.75	0.01
VIIZw403	-13.55	0.01	0.17	0.01	0.73	0.01	-1.39	26.09	0.00
Sm galaxies									
DDO 88	-13.67	0.01	2.20	0.01	-1.90	26.14	0.00
DDO 150	-15.04	0.00	0.21	0.01	1.27	0.01	-1.67	26.68	0.00
DDO 180	-17.36	0.00	1.83	0.00	-1.59	27.61	0.00
F583-1	-16.06	0.01	0.28	0.04	1.11	0.02	-1.78	27.09	0.00
NGC 2552	-15.94	0.00	0.15	0.00	1.40	0.00	-1.64	27.04	0.00
NGC 3109	-14.68	0.00	0.36	0.00	3.22	0.00	-1.68	26.42	0.00
NGC 3510	-15.93	0.00	0.45	0.01	1.34	0.00	-1.24	27.04	0.00

Notes.

^a M_{NUV} is an AB magnitude.

^b L_{NUV} here is in erg s^{-1} , as is $L_{\text{H}\alpha}$. L_{NUV} has been converted to erg s^{-1} by multiplying the flux in $\text{erg s}^{-1} \text{cm}^{-2}$ by the FWHM of the bandpass of the NUV filter in Angstroms.

^c From f_ν in $\text{erg s}^{-1} \text{Hz}^{-1}$.

that there is no attenuation in the outer disks of two dwarfs (IC1613, WLM), but uncertainties are large due to low *IRAS* fluxes.

Photometry in the largest ellipse yields integrated parameters, and differences between the ellipses divided by the area of the annulus give azimuthally averaged surface photometry. We fit the surface photometry with an exponential disk: $\mu^{\text{NUV}}(R) = \mu_0^{\text{NUV}} + 1.086R/R_D^{\text{NUV}}$, where R_D^{NUV} is the disk scale length measured in the NUV passband. The same quantity measured

in the *V* filter is denoted R_D^V . The fit was made with uniform weighting of each radial data point. Some galaxy profiles were better fit with two lines, as was sometimes also the case in the *V* band, and some profiles were not well fit by a straight line at all.

3. INTEGRATED PHOTOMETRY

In Table 3, we give the integrated UV photometry, including the NUV absolute magnitude M_{NUV} , the luminosity L_{NUV} ,

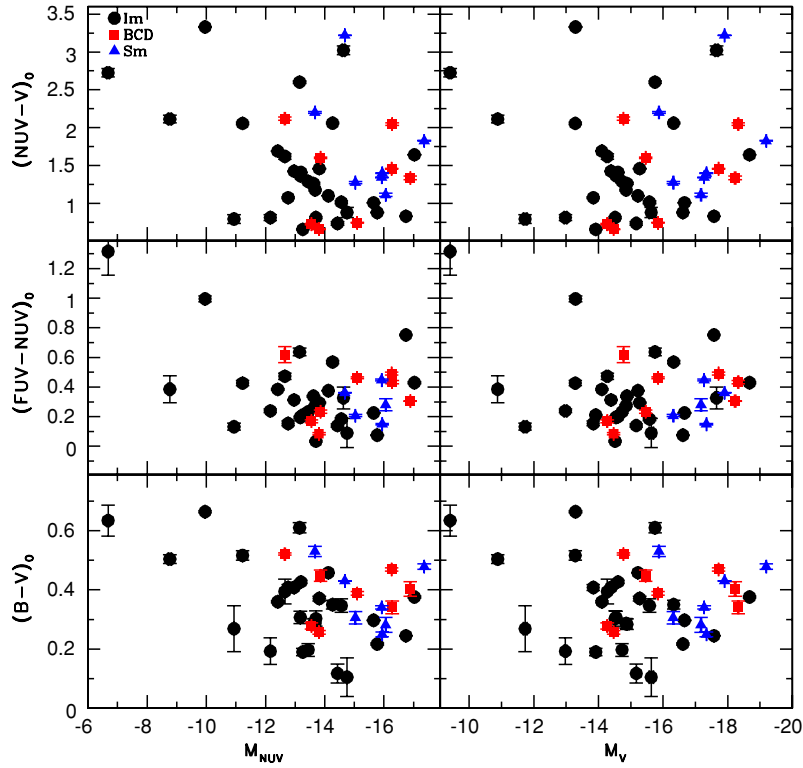


Figure 2. Integrated colors plotted against the absolute NUV AB magnitude (left) and absolute V magnitude (right). Colors are corrected for reddening. The dIm sample is shown as black filled circles, BCDs as red filled squares, and Sm galaxies as blue filled triangles. There is a rough trend of redder optical color for lower UV luminosity.

(A color version of this figure is available in the online journal.)

the color $(FUV - NUV)_0$, and the color $(NUV - V)_0$. Note that M_{NUV} is an AB magnitude, while magnitudes from the *UBV JHK* passbands are Vega magnitudes. All quantities are corrected for reddening. We also give the ratio $L_{H\alpha}/L_{NUV}$. The V-band and $H\alpha$ surface photometry are from Hunter & Elmegreen (2004, 2006).

In Figure 2, we plot $(FUV - NUV)_0$ and $(NUV - V)_0$, as well as $(B - V)_0$, against M_{NUV} and M_V . There is a rough trend of redder optical color for lower luminosity in the UV. However, the scatter is large and the low-luminosity end of the distribution is held down by just a few points. We do not see the trend of bluer UV-optical colors with lower luminosity found in studies of large samples of more massive galaxies (e.g., Wyder et al. 2007). In an integrated color-color plot (Figure 3) we do see a correlation: as a galaxy becomes redder in $(FUV - NUV)_0$, it also becomes redder in $(NUV - V)_0$.

Most of the galaxies have an integrated $(FUV - NUV)_0$ color between 0 and 0.5 mag. According to Thilker et al. (2005), a constant SFR stellar population would have an $(FUV - NUV)_0$ color of order -0.1 to 0 mag. So the dwarfs are generally redder than this model. However, the colors of most of the dwarfs are comparable to those of extinction-corrected colors of star-forming galaxies in the Goldmine sample as presented by Boissier et al. (2008). A few of the dwarfs have redder colors than this sample, and are comparable to the colors of low surface brightness galaxies of Boissier et al., which they interpret as most likely due to a variable star formation history. The BCDs in our sample cover the same range of integrated colors as the dIm galaxies. However, most of these galaxies have $(FUV - NUV)_0$ color gradients and are bluer in their centers, consistent with the central concentration of star formation that characterizes the BCD class of galaxies.

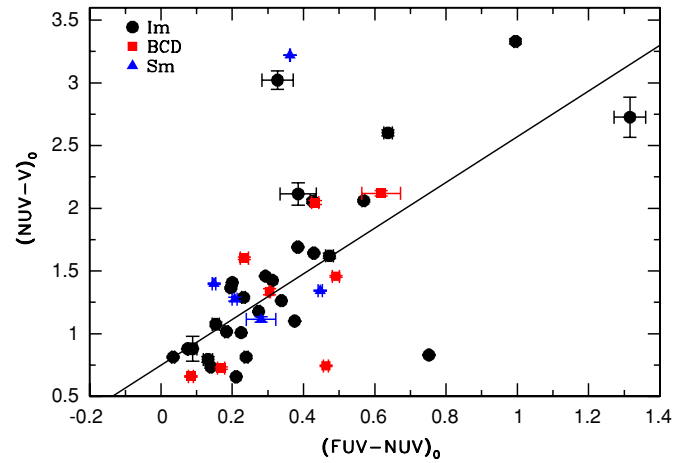


Figure 3. Integrated UV-optical color-color plot. Colors are corrected for reddening. The dIm sample is shown as black circles, BCDs as red squares, and Sm galaxies as blue triangles. The solid black line is a fit to all of the points except the four galaxies with the highest $(NUV - V)_0$: $(NUV - V)_0 = (0.75 \pm 0.12) + (1.82 \pm 0.27) \times (FUV - NUV)_0$. The two colors track each other.

(A color version of this figure is available in the online journal.)

4. SURFACE BRIGHTNESS PROFILES

The surface brightness profiles are shown in Figure 4. There we compare surface photometry in NUV, V, and $H\alpha$. The UV profiles extend beyond the $H\alpha$ profiles by at least two annuli in 66% (19 of 29) of the dIm, 75% (6 of 8) of the BCDs, and 71% (5 of 7) of the Sm galaxies. The uncertainty in these fractions

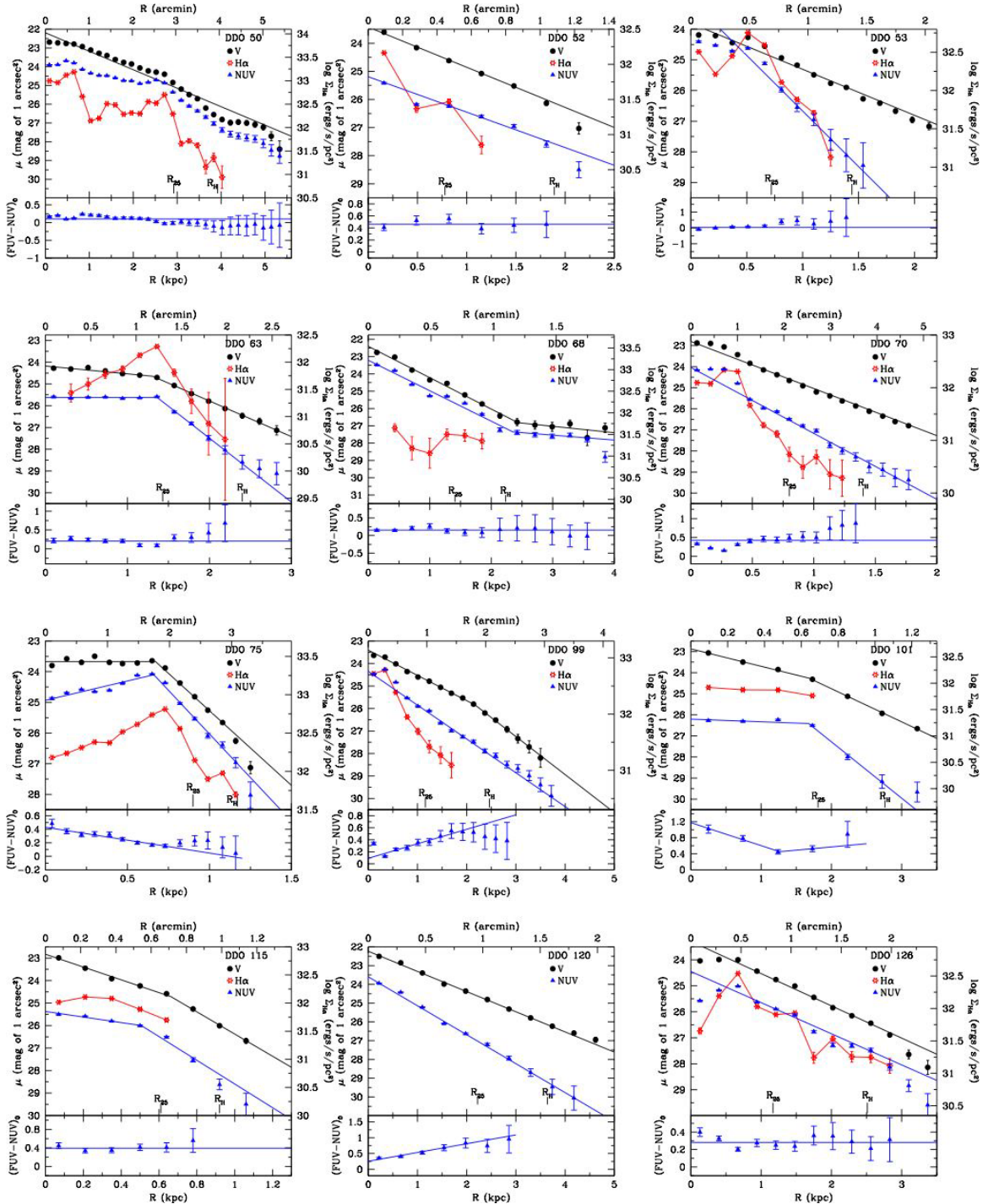


Figure 4. Azimuthally averaged surface brightness profiles in V (black), H α (red), GALEX NUV (blue), and (FUV – NUV)₀ (bottom panels). For NGC 3109, there is no V-band image, and a profile is shown instead for an H α off-band filter centered at 6440 Å with an FWHM of 95 Å. The radii R_{25} and R_H are marked. R_{25} is the radius at which the B -band surface brightness drops to 25 mag arcsec⁻². R_H is the Holmberg radius, the radius at which the B -band surface brightness drops to about 26.7 mag arcsec⁻².

(A color version of this figure is available in the online journal.)

(taken from the square root of the number of galaxies) in the BCD and Sm samples is of order 35%, while the uncertainty for the dIm galaxies is 19%. Four dIm galaxies without H α emission have UV emission; all of the galaxies have some UV emission.

We have fit the NUV surface photometry with exponential disk profiles, where appropriate, and the central surface brightness and disk scale lengths are given in Table 4. There are two

sets of entries in this table—measures of an inner profile and measures of an outer profile. Those galaxies whose profiles are best fit with a double exponential have two sets of numbers, while those that are fit just fine with a single exponential have entries only under the heading of “inner” profile. Of the 29 dIm galaxies, 8 have clear double exponential profiles in NUV; in 7 of these, the outer exponential drops more steeply than the inner, and in one the outer exponential is shallower. Three other

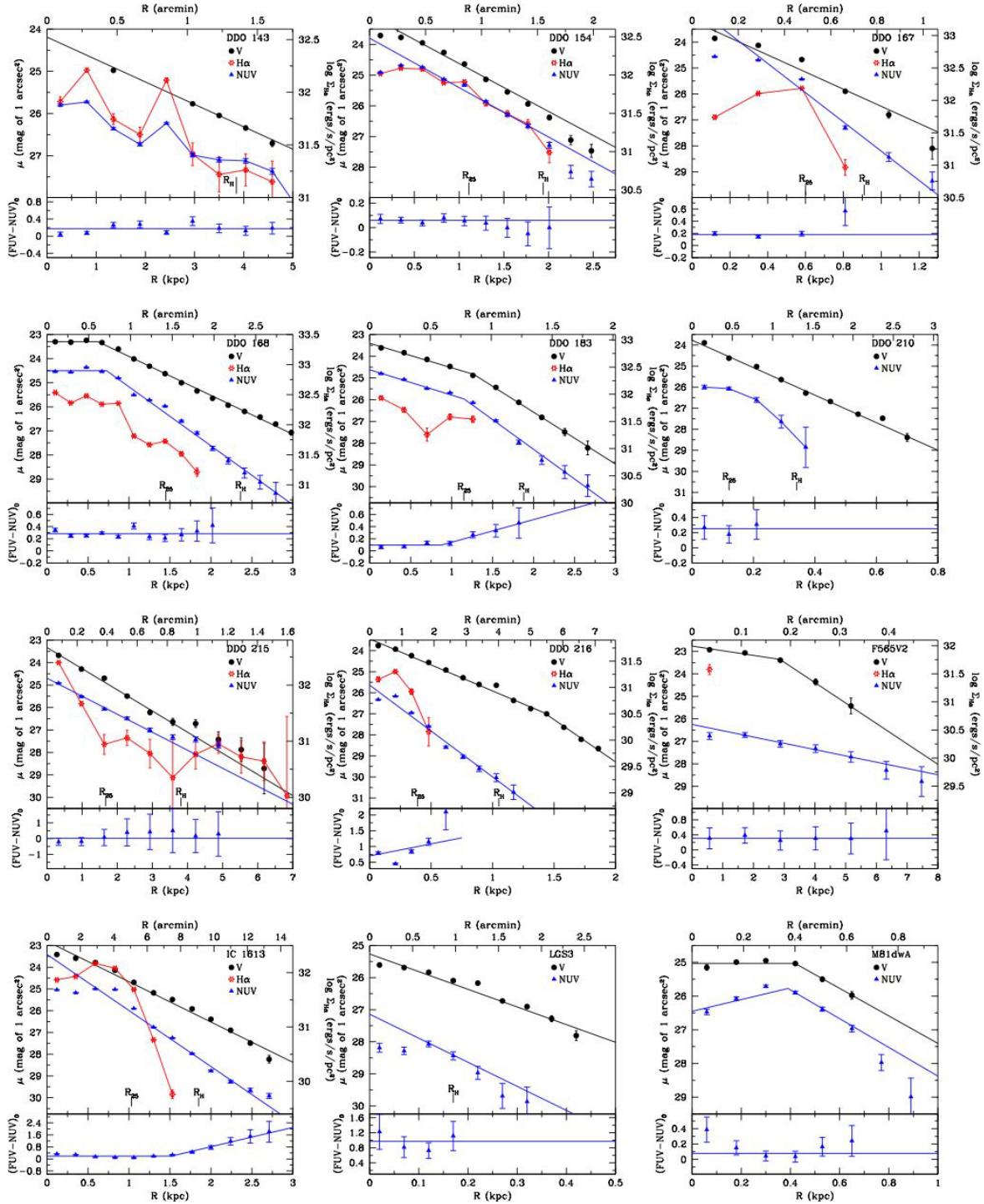


Figure 4. (Continued)

galaxies show breaks in V , but not in the UV. Of the eight BCDs, five have NUV double exponentials, all of which drop more shallowly in the outer disk. And, four of the seven Sms have profiles with breaks, all of which drop more steeply in the outer disk.

One galaxy, Haro 3, deserves individual mention. The UV image of Haro 3 was taken from archive combined images of unusual length. The NUV exposure altogether was 8.4 hr, and the FUV exposure was 3.5 hr rather than the typical exposure time of order half of an hour. Because of the unprecedented

(for extragalactic observations) exposure times, the signal to noise is superb and we are able to trace NUV to a surface brightness level of 29 mag of 1 arcsec². This is about twice as far in radius as our V -band and $H\alpha$ photometry go. In Figure 4, one can see that at the radius where V and $H\alpha$ end, the NUV surface photometry changes slope, becoming shallower. The break occurs at $2.3R_D^{\text{NUV}}$, where R_D^{NUV} is the disk scale length determined from the *outer* part of the profile. This type of double exponential is typical of many BCDs in optical and near-IR passbands, and the shallower outer profile is generally

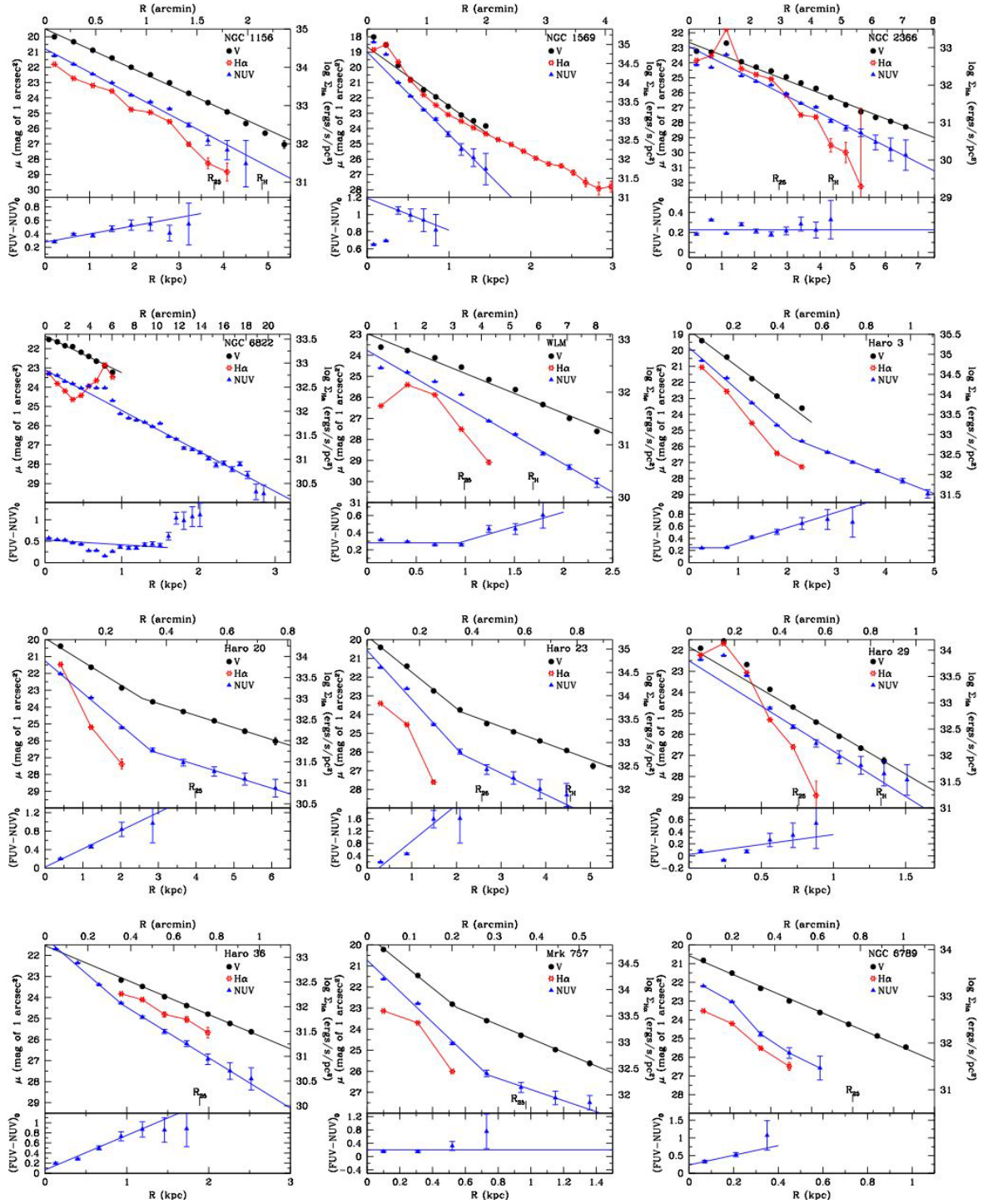


Figure 4. (Continued)

accepted as representing the underlying stellar population while the steeper inner profile is dominated by the intense recent star formation that is concentrated in the galaxy center (see, for example, Papaderos et al. 1996; Cairós et al. 2001; Noeske et al. 2003; Hunter & Elmegreen 2006). Consistent with this picture, we see in Figure 4 that $(FUV - NUV)_0$ is bluer in the inner part of the galaxy than in the outer parts, although the upturn to redder $(FUV - NUV)_0$ begins much closer to the center than the break in μ_{NUV} .

In Table 4, we give the V-band disk scale lengths R_D^V from Hunter & Elmegreen (2006) for comparison, and in Figure 5 we plot R_D^{NUV} against R_D^V . Symbol types indicate whether these scale lengths refer to the inner or outer disks. We see that the disk scale lengths in the two passbands are similar in most of the galaxies. Small galaxies, mostly Im and BCD, have slightly larger R_D^V than R_D^{NUV} , which means that their NUV emission and hence recent star formation is more centrally concentrated. Large galaxies,

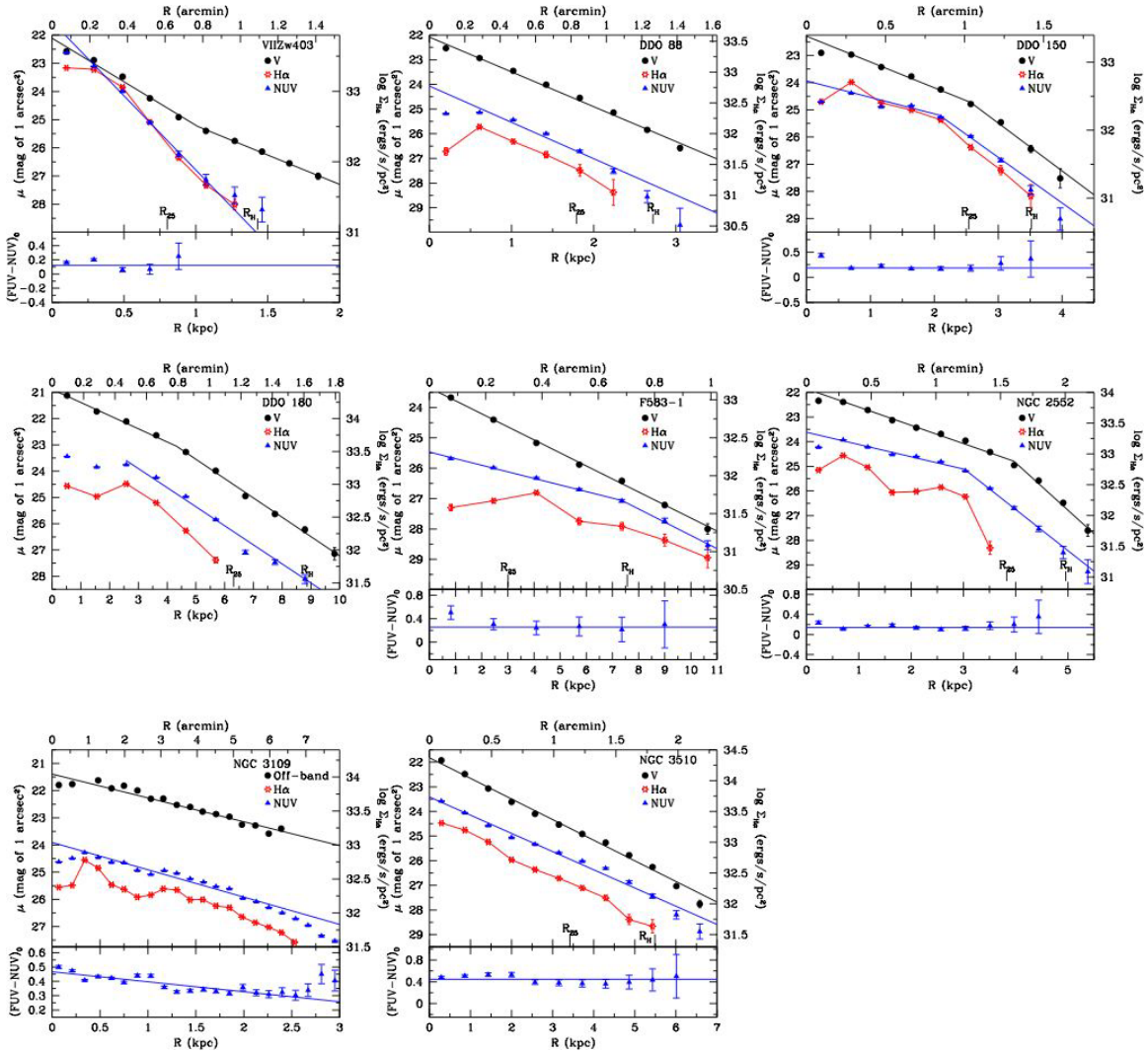


Figure 4. (Continued)

usually Sm, have slightly smaller R_D^V than R_D^{NUV} , which means their most recent star formation includes the outer disk.

In Figure 4, we include azimuthally averaged $(FUV - NUV)_0$ as a function of radius. Of the 29 dIm galaxies, 18 (62%) have constant colors as far as we measure both UV passbands, similar to low surface brightness galaxies (Boissier et al. 2008). However, seven (24%) dIm galaxies get redder with radius, one galaxy gets bluer, and three have color profiles that are too complex to put into one of these categories. Of the eight BCDs, on the other hand, six (75%) get redder with radius, as one would expect for centrally concentrated star formation, while two have constant colors. Interestingly, of the five Sm galaxies measured in both UV passbands, four have constant $(FUV - NUV)_0$ colors with radius and one profile gets slightly bluer with radius. The average $(FUV - NUV)_0$ colors, if constant, or color gradients are given in Table 5.

The double exponential profiles observed in μ_V and μ_{NUV} in some of our dwarfs are also seen in some spiral disks. Roskar et al. (2008) used simulations to argue that the break is a combination of reaching a star formation threshold in the outer disk and scattering of stars outward from the inner disk by spiral arms. This predicts that the stellar population in the outer disk is older than that in the inner disk since many of the stars did

not form there. Therefore, we expect a redder stellar population in the outer disk. This is not what we see in dIm galaxies. Most often colors in dIm galaxies are constant into the outer disk from the ultraviolet to the near-IR, and there is no correlation between dwarf galaxies that do show a color gradient and the presence of double exponential profiles. The surface brightness profile breaks, when present, are seen in all passbands from the UV to the near-IR (cf., Hunter & Elmegreen 2006; Hunter et al. 2006). Furthermore, dwarf irregulars do not have strong spiral arms, so the scattering mechanism proposed by Roskar et al. cannot operate in these systems. Stellar scattering in bar-like potentials might be important for some dwarfs, however.

5. INTEGRATED STAR FORMATION RATES

5.1. FUV, H α , and V-band Luminosities

We have converted the integrated photometry and azimuthally averaged surface photometry in the FUV, H α , and V band into SFRs. For the FUV, we use the formula from Kennicutt (1998) modified for the sub-solar metallicities appropriate for dwarf galaxies. Kennicutt's original formula is for Z_\odot . We used the stellar population evolution models of STARBURST99 (Leitherer et al. 1999) to determine the scaling from solar metallicity to sub-solar. Their Figure 54 plots the monochromatic

Table 4
Disk Structure

Galaxy	Inner						Outer					
	μ_0^{NUV} (mag arcsec $^{-2}$)	$\sigma_{\mu_0^{\text{NUV}}}$ (mag arcsec $^{-2}$)	$R_D^{\text{NUV}a}$ (kpc)	$\sigma_{R_D^{\text{NUV}}}$ (kpc)	R_D^V (kpc)	$\sigma_{R_D^V}$ (kpc)	μ_0^{NUV} (mag arcsec $^{-2}$)	$\sigma_{\mu_0^{\text{NUV}}}$ (mag arcsec $^{-2}$)	$R_D^{\text{NUV}a}$ (kpc)	$\sigma_{R_D^{\text{NUV}}}$ (kpc)	R_D^V (kpc)	$\sigma_{R_D^V}$ (kpc)
Im galaxies												
DDO 50	1.10	0.05
DDO 52	25.19	0.09	0.86	0.05	0.76	0.02
DDO 53	23.05	0.24	0.30	0.01	0.72	0.06
DDO 63	25.62	0.03	3.01	0.49	21.63	0.12	0.37	0.01	0.66	0.01
DDO 68	23.21	0.17	0.62	0.05	0.60	0.02	26.67	0.24	3.75	1.12	2.97	3.28
DDO 70	24.04	0.10	0.35	0.01	0.47	0.00
DDO 75	24.93	0.07	20.34	0.20	0.17	0.01	0.22	0.01
DDO 99	24.35	0.06	0.72	0.02	0.97	0.02	0.64	0.02
DDO 101	26.20	0.11	8.52	6.61	1.32	0.05	21.93	0.43	0.41	0.03	0.69	0.01
DDO 115	25.37	0.05	0.88	0.12	0.38	0.02	23.33	0.60	0.21	0.04	0.22	0.00
DDO 120	23.59	0.07	0.70	0.02	1.01	0.02
DDO 126	24.45	0.12	0.91	0.05	0.87	0.03
DDO 143	2.05	0.04
DDO 154	23.80	0.03	0.68	0.01	0.68	0.04
DDO 167	22.57	0.46	0.19	0.02	0.33	0.05
DDO 168	24.50	0.08	22.72	0.16	0.44	0.02	0.67	0.01
DDO 183	24.62	0.06	0.93	0.06	0.96	0.06	22.81	0.29	0.40	0.02	0.46	0.01
DDO 210	0.17	0.00
DDO 215	24.70	0.05	1.36	0.05	1.15	0.05
DDO 216	25.64	0.19	0.25	0.02	0.44	0.01	0.27	0.02
F565-V2	26.25	0.08	3.88	0.30	5.23	1.20	1.20	0.04
IC 1613	23.41	0.26	0.42	0.02	0.58	0.02
LGS3	27.14	0.00	0.14	0.00	0.20	0.01
M81dwA	26.45	0.24	24.11	0.00	0.26	0.00	0.27	0.00
NGC 1156	20.79	0.14	0.71	0.03	0.82	0.02
NGC 1569	19.00	0.14	0.20	0.01	0.28	0.01
NGC 2366	22.91	0.12	0.98	0.03	1.28	0.04
NGC 6822	23.10	0.08	0.52	0.01	0.57	0.03
WLM	23.77	0.16	0.40	0.01	0.57	0.03
BCD galaxies												
Haro 3	19.83	0.14	0.41	0.02	0.47	0.02	22.95	0.11	0.91	0.02
Haro 20	21.25	0.14	0.57	0.02	0.78	0.05	24.67	0.20	1.57	0.11	1.52	0.03
Haro 23	20.58	0.24	0.41	0.03	0.56	0.02	23.68	0.57	0.95	0.17	1.24	0.05
Haro 29	22.50	0.29	0.25	0.02	0.27	0.01
Haro 36	21.17	0.12	0.32	0.02	22.07	0.07	0.45	0.01	0.66	0.01
Mrk 757	20.73	0.22	0.15	0.01	0.17	0.00	24.23	0.30	0.41	0.05	0.33	0.01
NGC 6789	0.23	0.00
VIIZw403	21.53	0.10	0.21	0.01	0.52	0.01
Sm galaxies												
DDO 88	24.07	0.22	0.74	0.07	0.77	0.03
DDO 150	23.94	0.17	1.79	0.31	1.14	0.05	21.71	0.28	0.65	0.04	0.62	0.07
DDO 180	2.17	0.10	21.72	0.14	1.49	0.05	1.48	0.05
F583-1	25.47	0.03	5.00	0.14	2.53	0.06	23.85	0.31	2.49	0.20
NGC 2552	23.62	0.08	2.19	0.17	1.47	0.06	20.07	0.17	0.65	0.02	0.56	0.05
NGC 3109	23.91	0.09	1.08	0.06	1.24	0.09
NGC 3510	23.42	0.11	1.47	0.06	1.30	0.03

Note. ^a R_D are disk scale lengths. The disk scale lengths determined from the V-band R_D^V are from Hunter & Elmegreen (2006).

luminosity at 1500 Å as a function of time for a constant SFR stellar population with a Salpeter (1955) stellar initial mass function (IMF)—the function describing the number of stars of a given mass, and stellar masses 0.1–100 M_\odot . The effective wavelength of the FUV filter is 1516 Å, so using the luminosity at 1500 Å to examine the effect of metallicity is reasonable. The ratio of the luminosity for $Z = 0.008$ to that for Z_\odot is 1.10 at 100 Myr, and we have applied the inverse of this factor to Kennicutt’s proportionality constant to obtain the following:

$$\text{SFR}_{\text{FUV}} (M_\odot \text{ yr}^{-1}) = 1.27 \times 10^{-28} L_{\text{FUV}} (\text{erg s}^{-1} \text{ Hz}^{-1}).$$

The proportionality constant used here is 18% higher than the empirically determined relationship determined by Salim et al. (2007) for sub-solar (roughly 0.8 Z_\odot) metallicities in star-forming galaxies with a variety of star formation histories. On the other hand, our proportionality is 26% lower than that used by Thilker et al. (2007b), taken from Iglesias-Páramo et al. (2006) who used STARBURST99 models at solar metallicity.

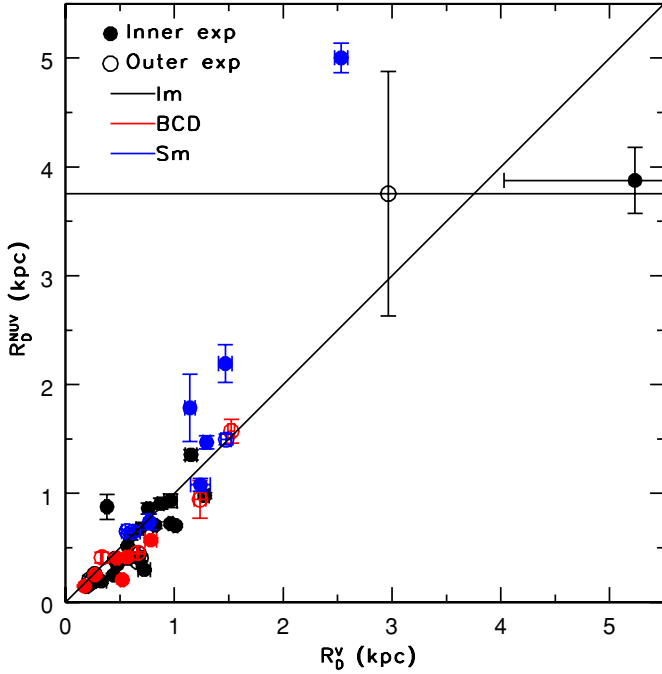


Figure 5. Disk scale length determined from NUV surface photometry compared to those determined from V-band surface photometry. For those profiles that were fit in two parts; the inner exponential is shown as a solid symbol, and the outer exponential disk scale length is shown as an open symbol. The Im sample is shown in black, BCDs as red, and Sm galaxies as blue.

For consistency in comparing SFRs, we also use Kennicutt’s (1998) formula for determining the SFR from $H\alpha$, modified again for non-solar metallicity. We scaled Kennicutt’s formula by the number of photons with wavelengths below 912 Å available for ionizing the gas using STARBURST99 (Leitherer et al. 1999). The ratio of the number of ionizing photons at $Z = 0.008$ to that at Z_{\odot} is 1.15, and we have applied the inverse of this factor to Kennicutt’s proportionality constant to obtain the following:

$$\text{SFR}_{H\alpha} (M_{\odot} \text{ yr}^{-1}) = 6.9 \times 10^{-42} L_{H\alpha} (\text{erg s}^{-1}).$$

Note that this formula produces a SFR that is 1.1 times higher than that which we derived and used for our larger optical survey (see Appendix B of Hunter & Elmegreen 2004). Thilker et al. (2007b) used a formula for solar metallicity, taken from Hirashita et al. (2003) and based on STARBURST99, that is the same as that of Kennicutt.

To determine the SFR averaged over a longer time scale, we use the V-band luminosity to determine the mass in stars and assume a timescale of 12 Gyr for the formation of that stellar mass. We use a stellar M/L_V ratio from Bell & de Jong (2001) that is a function of $(B - V)_0$ color: $\log(M/L_V) = -0.37 + 1.14(B - V)_0$. If there is no $(B - V)_0$ measurement or the uncertainty in the color is > 0.1 mag, we assumed $M/L_V = 1.07$ (appropriate for $(B - V)_0 = 0.35$). The Bell and de Jong relationship between mass-to-light ratio and color that we use is appropriate for a Salpeter (1955) stellar IMF and metallicity $Z = 0.008$, and is derived using the Bruzual & Charlot (2003) stellar population models. The SFR determined from the V band is the SFR necessary to produce the original mass in stars. The M/L_V formula gives us the mass currently in stars, and we correct this for the mass recycled back into

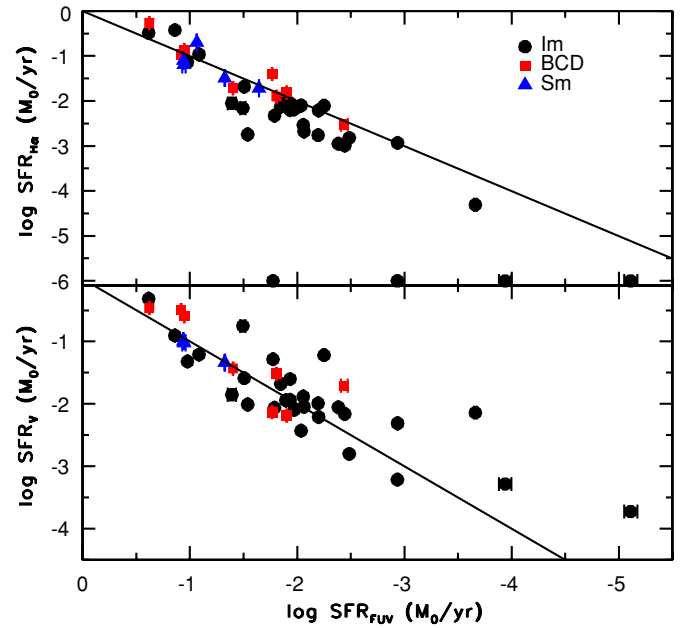


Figure 6. Integrated SFR determined from the FUV luminosity SFR_{FUV} plotted against the SFR determined from the V-band luminosity SFR_V and from the $H\alpha$ luminosity $\text{SFR}_{H\alpha}$. M_V is converted to mass in stars using a stellar M/L_V ratio, which depends on $(B - V)_0$, and the SFR_V assumes a constant SFR over 12 Gyr. Galaxies with no $H\alpha$ emission are plotted at $\log \text{SFR}_{H\alpha} = -6$. The solid black lines denote equal SFRs. The SFR_{FUV} are higher than $\text{SFR}_{H\alpha}$ for lower SFR systems, and lower than SFR_V for lower SFR systems.

the interstellar medium (ISM). We use a factor of 2 from Brinchmann et al. (2004) for this correction. The final formula for converting V band to an SFR is as follows:

$$\log \text{SFR}_V (M_{\odot} \text{ yr}^{-1}) = -0.4M_V + \log(M/L_V) - 7.842.$$

The integrated SFRs are given in Table 6, and plotted against each other in Figure 6. The integrated $\text{SFR}_{H\alpha}$ tends to be lower than SFR_{FUV} for some of the lower SFR dIm galaxies by a factor of 2.5 on average, but matches well for the lower SFR BCD and Sm galaxy sub-samples. At the high-SFR end, $\text{SFR}_{H\alpha}$ is a little high by a factor of up to 3 compared to SFR_{FUV} for several dIm, BCD, and Sm galaxies. On the other hand, the SFR determined from M_V , SFR_V , tends to be comparable on average to the current integrated SFR_{FUV} for all dwarf types except the very lowest SFR systems. There is, however, scatter around the relationship up to a factor of 3 for most of the galaxies. The low-SFR systems, on the other hand, have higher SFR_V than current integrated SFR_{FUV} . We consider the differences between these SFR measures in the following subsections.

5.1.1. Comparison of FUV and $H\alpha$

5.1.1.1. Extinction, calibration, and age effects. $\text{SFR}_{H\alpha}$ and SFR_{FUV} are both measures of recent star formation activity. Although they are sensitive to somewhat different timescales, we do expect these two SFR indicators to be fairly close. Here we consider possible reasons for the differences that we see.

Our first consideration is whether extinction errors contribute to the discrepancy between $\text{SFR}_{H\alpha}$ and SFR_{FUV} . The cause of the discrepancy is unlikely to be this simple given that our integrated $\text{SFR}_{H\alpha}$ are a little high at the high-SFR end while being too low at lower SFRs, but it is worth exploring. Treyer et al. (2007) have analyzed Sloan Digital Sky Survey and GALEX data on a large

Table 5
FUV – NUV Color Gradients

Galaxy	Inner					Outer			
	(FUV – NUV) ^{0a}	$\sigma_{(\text{FUV}-\text{NUV})^0}$	Gradient ^b (mag kpc ⁻¹)	σ_{gradient} (mag kpc ⁻¹)	$R_{\text{transition}}^c$ (kpc)	(FUV – NUV) ^{0a}	$\sigma_{(\text{FUV}-\text{NUV})^0}$	Gradient ^b (mag kpc ⁻¹)	σ_{gradient} (mag kpc ⁻¹)
Im galaxies									
DDO 50	0.10	0.08
DDO 52	0.46	0.07
DDO 53	0.03	0.07
DDO 63	0.20	0.07
DDO 68	0.15	0.06
DDO 70	0.42	0.05
DDO 75	0.43	0.02	-0.38	0.04
DDO 99	0.09	0.04	0.24	0.03
DDO 101	1.18	0.05	-0.57	0.06	1.26	0.25	...	0.16	...
DDO 115	0.39	0.04
DDO 120	0.25	0.03	0.28	0.03
DDO 126	0.28	0.07
DDO 143	0.18	0.10
DDO 154	0.06	0.01
DDO 167	0.18	0.02
DDO 168	0.28	0.06
DDO 183	0.10	0.03	0.88	-0.23	0.10	0.37	0.08
DDO 210	0.25	0.05
DDO 215	0.02	0.24
DDO 216	0.70	0.17	0.77	0.50
F565-V2	0.31	0.04
IC 1613	0.20	0.09	1.52	-1.74	0.28	1.28	0.15
LGS3	0.97	0.21
M81dwA	0.08	0.05
NGC 1156	0.28	0.03	0.12	0.02
NGC 1569	1.19	...	-0.37	...
NGC 2366	0.23	0.05
NGC 6822	0.53	0.03	-0.11	0.03
WLM	0.28	0.03	0.94	-0.03	0.24	0.34	0.19
BCD galaxies									
Haro 3	0.24	0.00	0.70	0.07	0.06	0.25	0.04
Haro 20	0.02	0.05	0.40	0.04
Haro 23	-0.30	0.42	1.17	0.41
Haro 29	0.02	0.12	0.33	0.30
Haro 36	0.06	0.06	0.69	0.09
Mrk 757	0.21	0.08
NGC 6789	0.23	...	1.38
VIIZw403	0.12	0.06
Sm galaxies									
DDO 88
DDO 150	0.19	0.02
DDO 180
F583-1	0.26	0.03
NGC 2552	0.14	0.03
NGC 3109	0.47	0.01	-0.07	0.01
NGC 3510	0.45	0.07

Notes.

^a Central color. An entry here and no entry under the gradient means that the color is constant.

^b (FUV – NUV)₀ color gradient. A color gradient without an uncertainty means that the central color and gradient were determined from only two points.

^c For profiles that are fit in two parts, this is the radius where the two fits cross.

sample of galaxies to determine integrated FUV extinctions and SFRs. They assume that extinctions determined from the Balmer decrement and SFRs determined from emission lines are most accurate. They then derive extinction formulae to make the UV-based SFRs come into agreement with the H α -based SFRs. The extinctions that their formulae imply for the dwarf galaxies are much higher than what we use here. On the other hand,

dust attenuation as a function of galactic mass determined from models give H α attenuations that are very close to those that we are using (Brinchmann et al. 2004). Furthermore, in both studies extinctions determined from the Balmer decrement are considered to be the best, and our average internal $E(B - V)_i$ for H α emission is derived from emission-line spectroscopy although a single average value is applied to all galaxies (Hunter

Table 6
Integrated Star Formation Rates

Galaxy	$\log \text{SFR}_{\text{FUV}}^{\text{a}}$ ($M_{\odot} \text{ yr}^{-1}$)	σ^{b} ($M_{\odot} \text{ yr}^{-1}$)	$\log \text{SFR}_{\text{H}\alpha}$ ($M_{\odot} \text{ yr}^{-1}$)	σ^{b} ($M_{\odot} \text{ yr}^{-1}$)	$\log \text{SFR}_{\text{V}}$ ($M_{\odot} \text{ yr}^{-1}$)	σ^{b} ($M_{\odot} \text{ yr}^{-1}$)	M/L_{V} ($M_{\odot}/L_{\text{V},\odot}$)	$\log \text{SFR}_{\text{FUV}}/\text{SFR}_{\text{H}\alpha}$	σ^{b}	$\log \text{SFR}_{\text{FUV}}/\text{SFR}_{\text{V}}$	σ^{b}
Im galaxies											
DDO 50	-0.98	0.00	-1.14	0.00	-1.32	0.00	0.75	0.16	0.00	0.34	0.00
DDO 52	-2.38	0.01	-2.95	0.01	-2.06	0.01	1.20	0.56	0.01	0.33	0.01
DDO 53	-2.20	0.01	-2.21	0.00	-2.21	0.00	1.25	0.01	0.01	0.01	0.01
DDO 63	-1.97	0.00	-2.18	0.01	-2.10	0.01	0.71	0.21	0.01	0.12	0.01
DDO 68	-1.54	0.00	-2.74	0.08	-2.01	0.01	0.58	1.21	0.08	0.47	0.01
DDO 70	-2.44	0.00	-2.99	0.00	-2.16	0.00	1.10	0.55	0.00	0.28	0.00
DDO 75	-2.04	0.00	-2.10	0.00	-2.43	0.00	0.70	0.06	0.00	0.39	0.00
DDO 99	-1.93	0.00	-2.20	0.01	-1.94	0.01	0.90	0.35	0.01	0.08	0.01
DDO 101	-2.25	0.01	-2.11	0.01	-1.22	0.00	2.12	0.14	0.01	1.03	0.01
DDO 115	-2.94	0.01	-2.93	0.01	-2.31	0.01	1.65	0.00	0.01	0.62	0.01
DDO 120	-1.77	0.00	-1.28	0.00	1.07	0.49	0.01
DDO 126	-1.89	0.00	-1.99	0.00	-1.94	0.00	0.91	0.10	0.00	0.05	0.00
DDO 143	-1.51	0.00	-1.68	0.01	-1.59	0.01	1.06	0.23	0.01	0.13	0.01
DDO 154	-1.79	0.00	-2.33	0.00	-2.06	0.01	0.94	0.54	0.01	0.27	0.01
DDO 167	-2.49	0.00	-2.82	0.01	-2.80	0.01	0.71	0.34	0.01	0.32	0.01
DDO 168	-1.85	0.00	-2.12	0.00	-1.68	0.00	1.13	0.28	0.00	0.17	0.00
DDO 183	-2.06	0.00	-2.68	0.02	-2.05	0.01	0.95	0.61	0.02	0.02	0.01
DDO 210	-3.94	0.06	-3.29	0.00	1.60	0.65	0.06
DDO 215	-1.39	0.04	-2.05	0.03	-1.85	0.03	0.55	0.66	0.05	0.46	0.05
DDO 216	-3.66	0.01	-4.31	0.07	-2.14	0.00	2.44	0.65	0.07	1.52	0.01
F565-V2	-1.49	0.02	-2.16	0.07	-0.75	0.02	1.07	0.74	0.07	0.67	0.02
IC 1613	-2.06	0.00	-2.53	0.00	-1.88	0.00	1.31	0.48	0.00	0.17	0.00
LGS3	-5.11	0.06	-3.73	0.01	2.25	1.38	0.06
M81dwA	-2.93	0.01	-3.21	0.02	0.86	0.32	0.02
NGC 1156	-0.62	0.00	-0.49	0.00	-0.31	0.00	1.14	0.13	0.00	0.30	0.00
NGC 1569	-0.86	0.00	-0.42	0.00	-0.90	0.00	0.81	0.44	0.00	0.05	0.00
NGC 2366	-1.09	0.00	-0.96	0.00	-1.21	0.00	0.93	0.12	0.00	0.13	0.00
NGC 6822	-1.93	0.00	-2.05	0.00	-1.60	0.00	1.42	0.12	0.00	0.33	0.00
WLM	-2.20	0.00	-2.76	0.00	-1.99	0.00	1.25	0.56	0.00	0.20	0.00
BCD galaxies											
Haro 3	-0.62	0.00	-0.26	0.00	-0.46	0.01	1.23	0.28	0.00	0.08	0.01
Haro 20	-0.92	0.00	-0.96	0.00	-0.50	0.01	1.04	0.04	0.00	0.42	0.01
Haro 23	-0.95	0.00	-0.87	0.00	-0.59	0.00	1.46	0.08	0.00	0.36	0.00
Haro 29	-1.77	0.00	-1.40	0.00	-2.13	0.00	0.84	0.34	0.00	0.40	0.00
Haro 36	-1.40	0.00	-1.72	0.00	-1.43	0.00	1.18	0.31	0.00	0.03	0.00
Mrk 757	-1.81	0.00	-1.90	0.00	-1.52	0.00	1.38	0.09	0.01	0.29	0.00
NGC 6789	-2.44	0.03	-2.53	0.01	-1.71	0.00	1.67	0.09	0.03	0.73	0.03
VIIZw403	-1.90	0.00	-1.81	0.00	-2.19	0.00	0.88	0.09	0.00	0.29	0.00
Sm galaxies											
DDO 88	-2.22	0.01	-1.26	0.00	1.72	0.46	0.01	0.50	0.00
DDO 150	-1.32	0.00	-1.49	0.00	-1.34	0.01	0.95	0.17	0.00	0.01	0.01
DDO 180	-0.49	0.00	0.01	0.00	1.50	0.21	0.00	0.29	0.00
F583-1	-0.94	0.02	-1.19	0.01	-1.02	0.01	0.89	0.25	0.02	0.08	0.02
NGC 2552	-0.94	0.00	-1.10	0.00	-0.99	0.00	0.82	0.16	0.00	0.05	0.00
NGC 3109	-1.64	0.00	-1.72	0.00	0.43	0.08	0.00
NGC 3510	-1.06	0.00	-0.70	0.00	-0.92	0.00	1.04	0.36	0.00	0.15	0.00

Notes.

^a Determined from FUV.

^b The σ refers to the uncertainty in the column to the left.

& Elmegreen 2004). In any event, increasing the extinction in the UV will not make the differences that we see go away since the UV-based SFRs are high compared to the $\text{H}\alpha$ -based SFRs. We would need instead to raise the extinction selectively to $\text{H}\alpha$ by 0.95 mag (0.37 mag in $E(B - V)_0$), but only in the lower SFR systems. Such high extinction values would be inconsistent with average Balmer decrements measured in dwarf galaxy H II regions.

Perhaps the difference between integrated $\text{SFR}_{\text{H}\alpha}$ and SFR_{FUV} is the result of an incorrect scaling coefficient for

converting $\text{H}\alpha$ or FUV luminosity relative to each other. The Brinchmann et al. (2004) models suggest that Kennicutt's (1998) scaling factor for converting $L_{\text{H}\alpha}$ to $\text{SFR}_{\text{H}\alpha}$ is a function of galaxy stellar mass. For the masses of our galaxies, a factor that is 0.7–0.8 times Kennicutt's scaling factor is suggested on average, similar to Salim et al.'s proportionality constant, which is 0.77 times Kennicutt's original value, for converting FUV to SFR_{FUV} . For $\text{SFR}_{\text{H}\alpha}$ we are scaling the original by 0.81 in order to account for the lower metallicity. Thus, we are using a formula that is similar to what others have derived for similar galaxies,

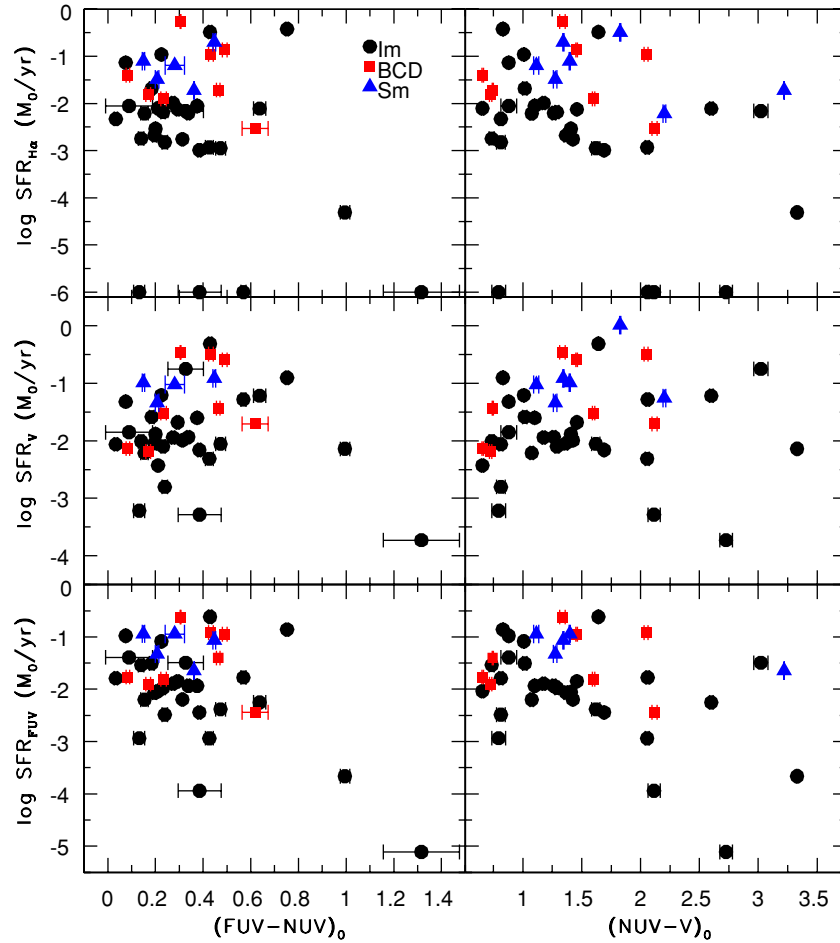


Figure 7. Integrated SFRs determined from $H\alpha$, the V -band luminosity, and the FUV luminosity plotted against the UV color (left) and UV-optical color (right). Galaxies with no $H\alpha$ emission are plotted at $\log \text{SFR}_{H\alpha} = -6$ (top). There is no trend of SFRs with these integrated galactic colors.

(A color version of this figure is available in the online journal.)

although there are certainly uncertainties. Furthermore, there is no correlation between our ratio $\text{SFR}_{\text{FUV}}/\text{SFR}_{H\alpha}$ and the oxygen abundance of the galaxy.

Could the difference between integrated $\text{SFR}_{H\alpha}$ and SFR_{FUV} be due to a larger contribution from older stars in galaxies where the SFR is lower? If that were the case, we would expect to see a correlation between the UV color $(\text{FUV} - \text{NUV})_0$ and the SFR_{FUV} . That is, as the SFR goes down, $(\text{FUV} - \text{NUV})_0$ should get redder ($\text{FUV} - \text{NUV}$ is a poor indicator of dust attenuation; Buat et al. 2005). Figure 7 is a plot of $(\text{FUV} - \text{NUV})_0$ and $(\text{NUV} - V)_0$ against our three luminosity-based SFR measures. There is not much of a trend of either color with any SFR. In spiral galaxies, FUV is considered a good measure of star formation activity for $\text{FUV} - \text{NUV} < 1$ (Boissier et al. 2007), and that is likely to be the case in dIm galaxies as well.

5.1.1.2. IMF effects. These considerations suggest that variable extinction, metallicity, and star formation history could contribute small differences between $\text{SFR}_{H\alpha}$ and SFR_{FUV} , but they are not likely to explain the full extent of the differences that we see. Another interesting possibility is that the difference between $\text{SFR}_{H\alpha}$ and SFR_{FUV} is the result of variations in the stellar IMF. Meurer et al. (2009) examined integrated $\text{SFR}_{H\alpha}$ and SFR_{FUV} for nearby galaxies and found a relationship between this ratio and the surface brightness in $H\alpha$. The relationship is such that galaxies with lower $H\alpha$ surface brightnesses have higher $\text{SFR}_{\text{FUV}}/\text{SFR}_{H\alpha}$ ratios. They suggested that this ratio is also

higher than that predicted by stellar population evolution models with constant SFRs, or by evolutionary histories with bursts or gasps in the SFRs. They concluded that the relationship is due to variations in the stellar upper mass limit or the slope of the stellar IMF.

We reproduce Meurer et al.'s (2009) relationship in the top panel of Figure 8. For $H\alpha$ surface brightness we use our integrated $H\alpha$ SFR and divide by the area over which $H\alpha$ was integrated. There is a clear correlation spanning four orders of magnitude in $\text{SFR}_{H\alpha}$ and one order of magnitude in $\text{SFR}_{\text{FUV}}/\text{SFR}_{H\alpha}$. Lower $H\alpha$ surface brightness corresponds to decreasing $H\alpha$ flux relative to FUV flux for all galaxy types in our survey. A power law fits this relationship well: $\text{SFR}_{\text{FUV}}/\text{SFR}_{H\alpha} \propto \text{SFR}_{H\alpha}^{-0.59 \pm 0.07}$. This result is similar to that in Meurer et al., which is $\text{SFR}_{\text{FUV}}/\text{SFR}_{H\alpha} \propto \text{SFR}_{H\alpha}^{-0.43 \pm 0.03}$. The bottom panel of Figure 8 shows no relationship between galactic M_V and $\text{SFR}_{\text{FUV}}/\text{SFR}_{H\alpha}$, so the $\text{SFR}_{H\alpha}$ correlation is only with surface brightness, not galaxy size. One can therefore imagine, following Meurer, et al., that surface brightness affects the IMF by producing proportionally more massive stars at higher interstellar pressures.

We also considered the IMF-dependent conversion from $H\alpha$ luminosity to SFR proposed by Pflamm-Altenburg et al. (2007, hereafter PWK). They suggested that the maximum stellar mass in a star cluster is determined by the total cluster mass, and that the maximum cluster mass in turn depends on the total SFR

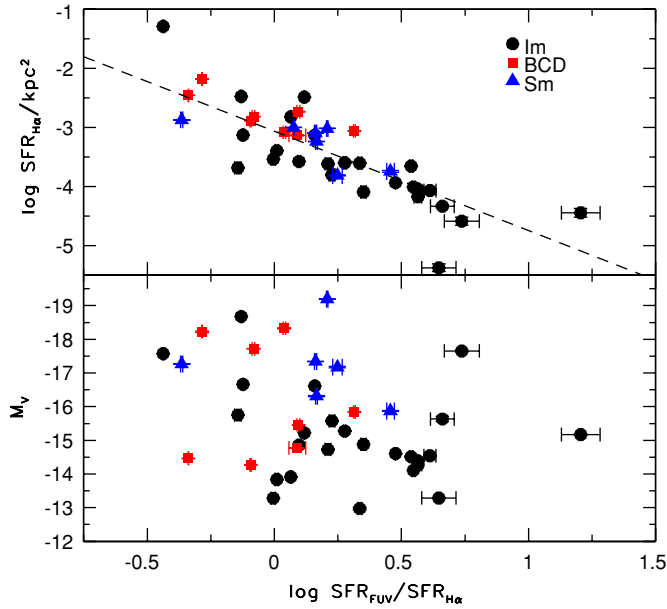


Figure 8. Ratio of integrated SFRs measured from the FUV to SFRs measured from $H\alpha$ vs. the $H\alpha$ SFR per unit area (top) and galactic M_V (bottom). The area used to normalize $SFR_{H\alpha}$ is that over which $H\alpha$ was measured. The dashed line in the upper panel is a fit to all but the three outlying points: $\log SFR_{H\alpha}/kpc^2 = -3.06 \pm 0.07 - (1.68 \pm 0.20) \times \log SFR_{FUV}/SFR_{H\alpha}$. (A color version of this figure is available in the online journal.)

of the system. Galaxy-wide IMFs should then be steeper than cluster IMFs, and they should be a function of the integrated SFR of the galaxy. As a result, the SFR should be higher for a given $H\alpha$ flux than it is with the standard IMF.

To compare our $H\alpha$ -based SFRs in Table 6 with the PWK rates, we computed new SFRs from our $H\alpha$ luminosities using their formula (17), which is a fifth-order polynomial fit for SFR as a function of $L_{H\alpha}$. The coefficients of the polynomial are listed in their Table 2 for several models, and we used the ones for their “standard” model. Their standard model is based on the “canonical IMF” given by their Equation (9): a power law with a Salpeter slope above $0.5 M_\odot$ and shallower at lower mass. A comparison between our $SFR_{H\alpha}$ from Table 6 and the Pflamm-Altenburg et al. SFR_{PWK} is shown in Figure 9. The Pflamm-Altenburg et al. prescription increases the $H\alpha$ -based SFR by a large factor. SFR_{PWK} is higher than our $SFR_{H\alpha}$ by a factor of 3 at high SFR, increasing to a factor of 45 at the lowest SFR (because of the very steep galaxy-wide IMFs used in the PWK model). The SFR_{PWK} are also higher than our SFR_V by a factor of order 3 on average, as shown in Figure 10. This discrepancy with the observations becomes even worse if we compare the PWK rate to SFR_{FUV} , which is lower than SFR_V at low surface brightness (Figure 6). Thus, the PWK prescription gives a SFR that is much higher than either the conventional $H\alpha$ or V-band rates, and these two rates are in better agreement with each other than with the PWK rates. In addition, PWK predicts a dramatic falloff in the traditional $SFR_{H\alpha}$ relative to SFR_{FUV} at low values of the true SFR (for example, with radius within a galaxy) that we do not see.

Generally, we hesitate to interpret the observed variations between $SFR_{H\alpha}$ and SFR_{FUV} in terms of a variable IMF. The basic problem is that the IMF also influences many other things, such as elemental ratios, color evolution, mass-to-light ratios, X-ray binary and pulsar fractions, and so on, and there is no evidence for these other variations yet. Another problem is that the correlation in Figure 8 is shallow and steady, unlike

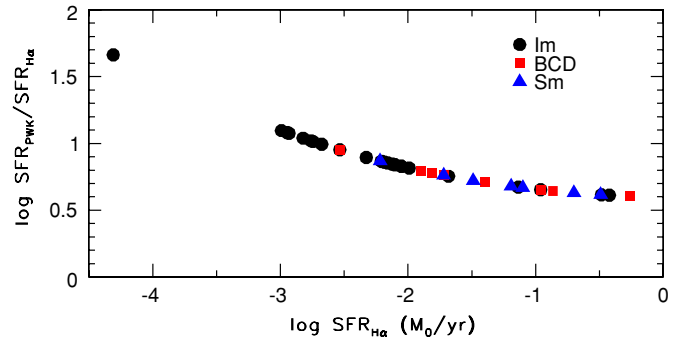


Figure 9. Ratio between integrated SFRs determined from $H\alpha$ luminosities $SFR_{H\alpha}$, as given in Table 6, and from the prescription of Pflamm-Altenburg et al. (2007) SFR_{PWK} . The Pflamm-Altenburg et al. formula is a function of the SFR itself, and the difference between our adopted conversion method and that of Pflamm-Altenburg et al. increases as the SFR decreases, with SFR_{PWK} being higher than $SFR_{H\alpha}$ by factors of up to 45. (A color version of this figure is available in the online journal.)

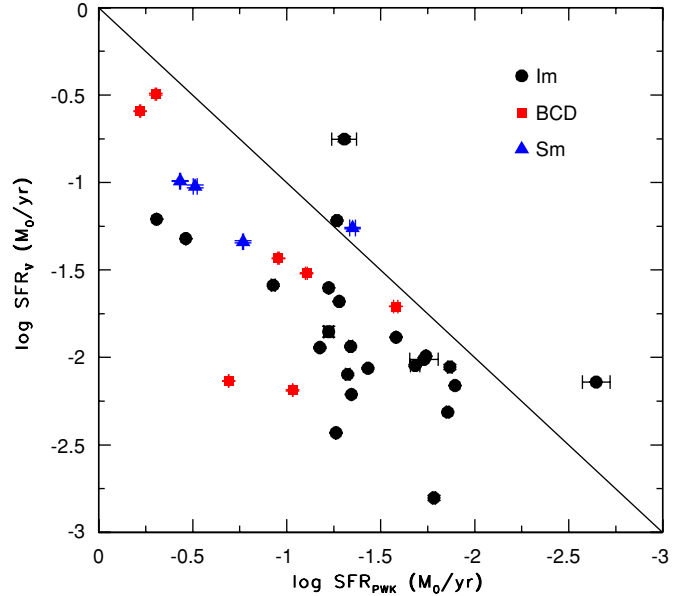


Figure 10. Comparison of the SFR determined from $H\alpha$ luminosities following the prescription of Pflamm-Altenburg et al. (2007) SFR_{PWK} and the SFR determined from M_V SFR_V . The slanting solid line marks equal SFRs. The Pflamm-Altenburg et al. prescription exacerbates the discrepancy between the $H\alpha$ -based SFR and the SFR determined from M_V . (A color version of this figure is available in the online journal.)

the correlation between stellar mass and the ratio of FUV flux to Lyman continuum flux (shown in Figure 10 of Meurer et al. 2009), which should produce more of a threshold effect. Finally, the correlation between $SFR_{FUV}/SFR_{H\alpha}$ and $SFR_{H\alpha}$ for whole galaxies (Figure 8) is analogous to the correlation between $SFR_{FUV}/SFR_{H\alpha}$ and galactocentric radius in each galaxy (Figures 14–16), where at larger radii there is a shift toward lower $H\alpha$ surface brightness and higher $SFR_{FUV}/SFR_{H\alpha}$ ratio.

These considerations lead us to believe that the IMF and star formation properties in these galaxies are not abnormal because of the PWK cluster-sampling effect. Cluster-sampling anomalies also appear to be ruled out by the cluster birth line in a plot of $L_{H\alpha}/L_{Bol}$ versus L_{Bol} for M33 clusters (Corbelli et al. 2009). Still, there could be other reasons for bottom-heavy IMFs in low surface brightness regions. The pressure

and density are low in these regions, and this may affect the upper stellar mass limit or the upper mass IMF slope in physical ways, independently of the star cluster mass or the total number of clusters in a galaxy (e.g., Elmegreen 2004). In the PWK model, the upper stellar mass depends rigorously on the cluster mass (rather than in an average sense only), and the upper cluster mass depends rigorously on the number of clusters in the galaxy (again, as distinct from the average dependence seen by Whitmore 2003).

In addition, a considerable fraction of the diffuse H α around massive stars should be too faint to see when the surface brightness is low (Elmegreen & Hunter 2006). For example, Melena et al. (2009) found a significant lack of H α from UV-bright star-forming regions in the outer parts of a sub-sample of the galaxies studied here. They showed that Strömgren radii around even single massive stars can be comparable to or larger than the gaseous scale height. Then a high fraction of the Lyman continuum photons can escape the galaxy and what remains can produce an ionized medium that is too low in emission measure to observe by present-day techniques. Galaxies with low SFRs could have a lot of leakage because these galaxies have low gas surface densities, low pressures, and low densities for the absorption of ionizing photons. They might also have more blow out of their interstellar gas near star-forming regions because of the low binding energy of the disk. On the other hand, if the fraction of star formation in a clustered form is lower in low-pressure environments (e.g., Elmegreen 2008; Elias et al. 2009), then the ISM blow out may be less concentrated in dwarfs.

The correlations between $\text{SFR}_{\text{FUV}}/\text{SFR}_{\text{H}\alpha}$ and $\text{SFR}_{\text{H}\alpha}$ in Figure 8 and in Meurer et al. (2009) can be explained if H α fills the whole disk thickness in the patches where O star ionization occurs. We think of this as *saturated ionization*. An important consideration is the gas disk thickness, which is about constant from galaxy to galaxy. The H α surface brightness is generally proportional to the emission measure, $n_e^2 L$ for electron density n_e and H II region depth L . When ionization fills the disk thickness, L is this thickness and n_e is the average ISM density, n_{gas} . Thus, H α surface brightness scales with n_{gas}^2 if L is about constant. The SFR per unit area determined from H α is directly proportional to the H α surface brightness, and therefore to n_{gas}^2 too, in this saturated case. Such a $\text{SFR}_{\text{H}\alpha} - n_{\text{gas}}^2$ relation is not the Kennicutt relation nor is $\text{SFR}_{\text{H}\alpha}$ in this case really proportional to the SFR. It is just a measure of the total emission measure in a highly ionized, and perhaps leaky, patch of the ISM. The SFR would be larger than what is derived from the Kennicutt relation using H α if Lyman continuum photons escape through the top and bottom of the disk. At the same time, the FUV SFR probably scales with the ISM density to some power, n_{gas}^γ for $\gamma \sim 1$ to ~ 1.5 , depending on molecular fraction. This is the relation discussed by Kennicutt (1998), Wong & Blitz (2002), Leroy et al (2008), and others, but written in terms of density rather than column density; for constant L . Eliminating n_{gas} yields $\text{SFR}_{\text{FUV}}/\text{SFR}_{\text{H}\alpha} \propto \text{SFR}_{\text{H}\alpha}^{\gamma/2-1}$. For $\gamma = 1$ or 1.5 , $\text{SFR}_{\text{FUV}}/\text{SFR}_{\text{H}\alpha} \propto \text{SFR}_{\text{H}\alpha}^{-0.5}$ or $\text{SFR}_{\text{H}\alpha}^{-0.25}$, respectively. These two power laws span the relationship shown in Figure 8.

In the far-outer parts of disks, the thickness should increase in a typical flare and then the local ISM density should begin to drop more quickly, making the emission measure around a typical O-type star drop suddenly as well (Elmegreen & Hunter 2006) and the escape of Lyman continuum photons even more likely.

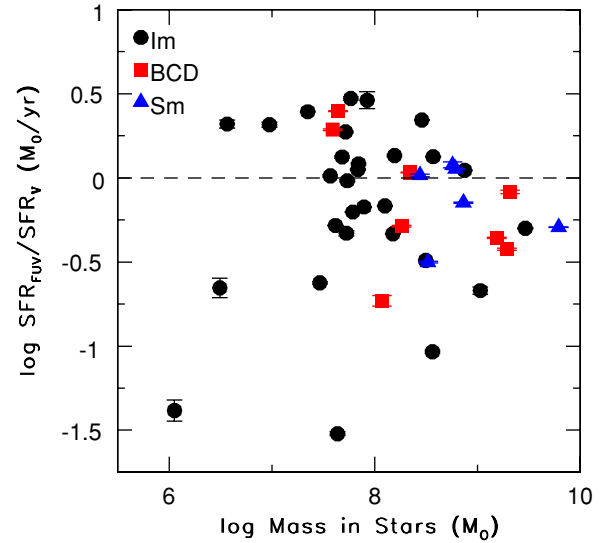


Figure 11. Ratios $\text{SFR}_{\text{FUV}}/\text{SFR}_V$ as a function of integrated galactic mass in stars. The mass in stars is determined from M_V and M/L_V as described in the text. The dashed horizontal line marks a ratio of 1. This plot is used to explore the possibility that the SFRs based on total mass over estimate the bulk age of the galaxy as a function of mass of the galaxy, an idea proposed by Bell & Bower (2000).

(A color version of this figure is available in the online journal.)

5.1.2. Comparison of FUV and V

The SFR_V is a measure of the average SFR over a much longer timescale than that measured by FUV. Figure 6 shows that SFR_{FUV} and SFR_V are comparable on average for most of the galaxies, but with a large scatter about the relationship. The equivalence of the SFRs at two different timescales implies that, on average, the SFR is constant in most dwarf galaxies. The large scatter around the relationship implies that integrated SFRs may vary routinely by factors of a few. This is consistent with the notion of “gasping” star formation histories determined from color-magnitude diagrams of nearby dwarfs in which the SFR varies by factors of a few over long periods of time (for example, Marconi et al. 1995). We consider this level of variability in the SFR to be due to statistical variations in star formation in a small galaxy.

Although SFR_V is similar to SFR_{FUV} , there is one particular uncertainty in SFR_V that merits discussion. The SFR_V has been derived by computing the mass in stars and dividing by a constant age of 12 Gyr. But, Bell & Bower (2000) and Bell & de Jong (2001) found that the best fits to colors and color profiles for spirals come from models in which the bulk of the disk formation epoch is a function of the halo mass of the galaxy. According to these studies, galaxies with total masses of order $10^{13} M_\odot$ have ages of 12 Gyr, but galaxies with masses of order $10^9 M_\odot$ have effective ages of order 4 Gyr in the sense that this is the timescale over which the bulk of stars have formed. Using an age of 4 Gyr would increase the SFR_V by a factor of 3 or 0.48 in the logarithm of the rate. If generally applied to all dwarfs, this factor would then make SFR_V larger on average than the current SFR by a corresponding factor of 3. To explore this idea, we plot the galactic stellar mass against the ratio of SFR_{FUV} to SFR_V in Figure 11. The stellar mass is from M_V and M/L_V . We see that the SFR_V is too low relative to SFR_{FUV} by a factor of up to 3 (up to 0.5 in the log) for some galaxies, and too high by up to a factor of 30 (1.5 in the log) for others. The galaxies requiring higher SFR_V , which are mostly systems with masses $\leq 10^9 M_\odot$,

would benefit from a lower galactic age. Thus, a lower effective galaxy age for some systems is possible, although there is no clear trend with mass. On the other hand, for the galaxies with SFR_V that are too high relative to SFR_{FUV} , a much greater age does not solve the problem, and instead an alternate form for the star formation history would make more sense, requiring the current SFR to be lower than the average past rate. We explore the effects of star formation histories on integrated SFRs in the following section.

5.2. Color Modeling

We have modeled a simple evolutionary history of our galaxies using population synthesis fitting of integrated UV, optical, and near-IR colors, as available, given in Tables 2 and 3. We used the library of stellar populations from Bruzual & Charlot (2003), choosing the “Padova (1994)” stellar evolutionary tracks (Alongi et al. 1993; Bressan et al. 1993; Fagotto et al. 1994a, 1994b) and a Salpeter (1955) stellar IMF. We also used the oxygen abundances of our galaxies to choose the spectral synthesis models, $Z = 0.0004, 0.004$, or 0.008 , that are closest to the observed metallicities. If no oxygen abundance was available, we used the M_B of the galaxy and Richer & McCall’s (1995) relationship between M_B and O/H for dwarfs to estimate the proper metallicity choice. The chosen model Z is given in Table 7.

We fit the colors for each galaxy with a constant SFR model and a declining SFR with six different decay times— 10^{10} yr, 10^9 yr, 7×10^8 yr, 3×10^8 yr, 10^8 yr, and 10^7 yr. Declining star formation models assume that the SFR was higher in the past, which is true for the universe in general as a result of higher relative gas fractions and galaxy interaction rates. Our modeling program loops over age and finds model colors. For each model color we subtract the observed color and divide the difference by the uncertainty in the measured color. We then sum the square of this difference over the colors. This is a χ^2 . Among all possible solutions, we then average with an $\exp(-0.5\chi^2)$ weighting factor to obtain a final age and mass. The uncertainties in many of our colors are sufficiently small compared to the model SED fits that the χ^2 values were unreasonably large (often greater than 40). So, we multiplied all of the color uncertainties by a constant factor of 20 for all galaxies in order to get non-zero Gaussian weights. This is effectively the same as considering greater than statistical uncertainties, or systematic uncertainties, in the observations and models. In a small number of cases, the χ^2 method does not find a good solution at all. We considered this to be the case when 5 or fewer of the age models out of the 164 trial ages in the Bruzual & Charlot tables gave $\chi^2 < 40$. We then modified our method to obtain the best possible SED fit by averaging together the trial ages and masses from only those age trials that had the lowest rms deviation between the observed and modeled colors (i.e., not dividing by the measurement errors as in the χ^2 method). The weights for this average were taken to be Gaussian functions of this rms deviation, rather than χ^2 . The uncertainties in the results for these cases were taken from the rms values in the averages. Of the seven models for each galaxy, we chose the one that best fits the galaxy colors.

The SFR, SFR_{Col} , is taken to be the color-derived mass in stars divided by the color-derived age of the galaxy for the best-fit model. We correct the model mass for the mass recycled back into the ISM by increasing the mass by a factor of 2 (Brinchmann et al. 2004). The best-fit model parameters are given in Table 7.

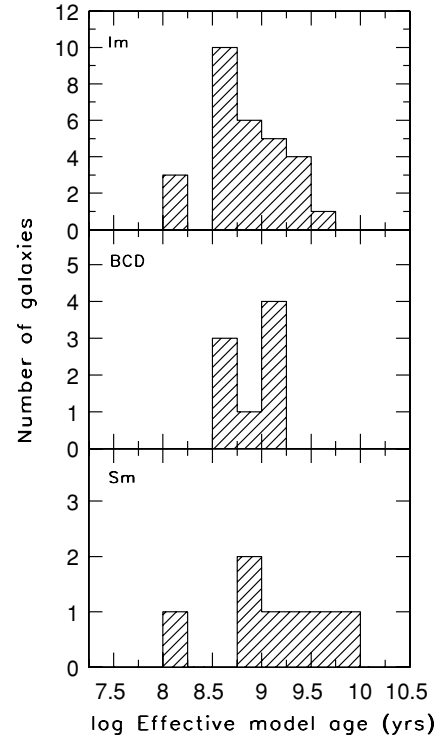


Figure 12. Histogram of effective galactic ages from models of the integrated colors.

The color-derived age is approximately the time when the most prominent burst of star formation occurred. The corresponding SFR is the average since that time. Generally, we expect SFR_{Col} to be larger than SFR_V because any burst reflected by SFR_{Col} will be stronger than the average rate over a Hubble time, as reflected by SFR_V . Similarly, SFR_{Col} will be larger than SFR_{FUV} if there has been some decay in the SFR over the last several gigayears.

A histogram of the color-derived ages is shown in Figure 12. The ages cluster around 1 Gyr, with a few larger values for Im and Sm types than for BCD types. This gigayear color-derived age means that most of the optical light in these galaxies comes from star formation within the last gigayear. The fact that BCDs have color ages that are similar to those of the other types implies that BCDs are not undergoing a recent and global burst, lasting only 100 Myr, for example. The intense inner disk activity in BCDs may be somewhat recent, as suggested by its relatively blue color, but the whole disk SFR has to be sustained for a gigayear or more. This means that the Im and Sm types differ from BCDs primarily in the former’s lack of spatial concentration for the most recent star formation.

In Figure 13, we compare SFR_{Col} to the SFRs determined from the V band and FUV. We see that SFR_{Col} is indeed greater than both of these SFR measures—by a factor of about 5 on average. As discussed above, this factor follows from the exponential star formation history that we have fit to the optical colors. With this history, the instantaneous SFR is $S(t) = S_0 \exp(-t/t_d)$ for rate normalization S_0 , time t from some past beginning, and decay time t_d . The total mass is $\int_0^{\text{age}} S(t) dt$, and the average rate is this mass divided by the age. Writing $\xi = \text{age}/t_d$, the average rate becomes $S_0(1 - e^{-\xi})/\xi$. The rate today is much smaller than this, $S_0 e^{-\xi}$. The ratio of the past average divided by the today’s rate is $(e^{\xi} - 1)/\xi$. Figure 13 indicates a value of ~ 5 for this SFR ratio, which implies $\xi \sim 2.7$ or $\log \xi \sim 0.43$. The average value of $\log \xi$ in Table 7 is

Table 7
Model Fits to Integrated Colors

Galaxy	Model Z	log Decay t ^a (yr)	log Age (yr)	σ	log Mass (M_{\odot})	σ	log SFR _{Col} ^b (M_{\odot}/yr)	σ	N _{mod} ^c	rms _{mod} ^d	$\Delta(\text{FUV} - \text{NUV})^e$	$\Delta(U - B)^e$	$\Delta(B - V)^e$	$\Delta(J - H)^e$	$\Delta(H - K)^e$
Im galaxies															
DDO 50	0.0040	7.00	8.12	0.07	7.78	0.03	-0.04	0.05	0	0.15	-0.02	0.19	-0.09
DDO 52	0.0040	9.00	8.75	1.04	7.11	0.71	-1.34	0.05	0	0.35	-0.40	-0.21	-0.07
DDO 53	0.0040	0.00	9.47	0.69	7.15	0.40	-2.02	0.30	6	0.45	-0.27	0.30	-0.10	0.03	...
DDO 63	0.0004	8.00	8.69	0.24	7.31	0.16	-1.07	0.05	0	0.05	-0.04	0.00	-0.02
DDO 68	0.0004	8.85	8.73	0.79	7.44	0.42	-0.99	0.60	3	0.25	-0.20	-0.11	0.04
DDO 70	0.0004	8.48	9.16	0.05	7.34	0.05	-1.52	0.05	0	0.05	0.01	-0.02	0.03
DDO 75	0.0004	8.00	8.72	0.06	7.01	0.05	-1.41	0.25	2	0.35	-0.01	0.39	-0.01
DDO 99	0.0040	8.00	8.74	0.07	7.42	0.06	-1.02	0.05	0	0.15	-0.04	0.17	0.02
DDO 101	0.0080	8.85	9.51	0.49	8.36	0.46	-0.85	0.05	1	0.25	-0.08	0.11	0.05
DDO 115	0.0080	8.48	8.89	0.47	6.84	0.35	-1.75	0.05	0	0.15	-0.12	0.02	-0.12
DDO 120	0.0040	8.00	8.80	0.13	8.05	0.10	-0.46	0.05	0	0.15	-0.10	0.10	0.00
DDO 126	0.0040	8.00	8.68	0.13	7.35	0.11	-1.03	0.05	1	0.25	-0.06	0.28	-0.01
DDO 143	0.0040	8.85	8.65	0.79	7.50	0.52	-0.85	0.34	6	0.55	-0.24	0.46	-0.10
DDO 154	0.0040	0.00	9.48	0.73	7.43	0.42	-1.75	0.21	5	0.15	-0.15	0.10	0.01
DDO 167	0.0004	8.48	8.65	0.67	6.55	0.38	-1.80	0.28	3	0.25	-0.19	0.07	-0.03
DDO 168	0.0040	8.48	9.04	0.05	7.70	0.04	-1.04	0.05	1	0.45	-0.06	0.22	0.03	0.16	-0.40
DDO 183	0.0040	8.48	8.78	0.41	7.20	0.29	-1.28	0.15	2	0.15	-0.14	0.04	-0.03
DDO 210	0.0004	9.00	9.48	0.60	6.24	0.43	-2.94	0.05	1	0.05	0.55	-0.08	-0.06
DDO 215	0.0080	9.00	8.20	1.23	7.38	0.83	-0.52	0.49	2	0.25	-0.06	-0.01	0.07
DDO 216	0.0040	8.48	9.26	0.05	7.14	0.07	-1.82	0.05	1	0.15	0.07	0.10	-0.07
F565-V2	0.0040	8.85	8.17	1.22	8.15	0.81	0.28	0.18	3	0.05	-0.18
IC 1613	0.0040	8.48	9.06	0.00	7.45	0.00	-1.30	0.05	1	0.15	0.06	-0.16	-0.02
LGS3	0.0004	8.85	8.65	1.24	5.21	0.73	-3.14	0.22	2	0.15	-0.57	-0.46	-0.42
M81dwA	0.0004	0.00	8.72	1.24	6.03	0.60	-2.39	0.43	2	0.25	-0.33	-0.14	-0.17
NGC 1156	0.0080	8.00	8.72	0.06	8.96	0.05	0.54	0.27	2	0.35	-0.06	0.28	-0.08	-0.06	0.05
NGC 1569	0.0040	8.00	8.86	0.04	8.59	0.03	0.03	0.05	0	0.65	-0.17	0.59	0.13	-0.10	0.14
NGC 2366	0.0040	8.48	8.83	0.12	8.06	0.11	-0.47	0.31	4	0.35	-0.22	0.23	-0.04	0.09	0.11
NGC 6822	0.0040	8.48	9.06	0.04	7.69	0.02	-1.06	0.26	2	0.35	-0.10	0.33	-0.04
WLM	0.0040	8.48	9.07	0.03	7.37	0.01	-1.40	0.05	0	0.15	-0.01	-0.18	0.03
BCD galaxies															
Haro 3	0.0080	8.48	9.06	0.02	8.95	0.01	0.19	0.41	6	0.45	-0.02	0.46	0.04	-0.12	...
Haro 20	0.0080	8.48	9.05	0.23	8.98	0.19	0.23	0.05	0	0.15	-0.06	-0.06	0.12
Haro 23	0.0080	8.48	9.07	0.10	8.75	0.09	-0.02	0.05	1	0.45	-0.15	0.25	-0.01	-0.36	...
Haro 29	0.0040	8.85	8.69	0.36	7.00	0.23	-1.38	0.34	6	0.35	-0.20	0.21	-0.09	-0.09	...
Haro 36	0.0080	8.00	8.75	0.05	7.85	0.05	-0.60	0.05	1	0.15	-0.02	0.07	-0.07
Mrk 757	0.0040	8.48	8.62	0.59	7.46	0.40	-0.86	0.37	3	0.25	-0.20	0.05	-0.21
NGC 6789	0.0040	8.48	9.18	0.09	7.64	0.10	-1.24	0.05	0	0.15	0.10	0.18	0.01
VII Zw 403	0.0004	8.48	8.88	0.28	7.18	0.19	-1.40	0.49	6	0.35	-0.11	0.26	-0.08

Table 7
(Continued)

Galaxy	Model Z	log Decay t ^a (yr)	log Age (yr)	σ	log Mass (M_{\odot})	σ	log SFR _{Col} ^b (M_{\odot}/yr)	σ	N _{mod} ^c	rms _{mod} ^d	$\Delta(\text{FUV} - \text{NUV})^e$	$\Delta(U - B)^e$	$\Delta(B - V)^e$	$\Delta(J - H)^e$	$\Delta(H - K)^e$
Sm galaxies															
DDO 88	0.0040	9.00	9.27	0.84	8.13	0.65	−0.84	0.50	3	0.05	...	0.01	−0.03
DDO 150	0.0080	8.48	8.82	0.34	7.97	0.26	−0.54	0.60	4	0.25	−0.11	0.13	−0.02
DDO 180	0.0080	0.00	9.80	0.37	9.54	0.24	0.04	0.05	1	0.15	...	0.00	−0.10	−0.17	...
F583-1	0.0040	9.00	8.20	1.10	7.91	0.70	0.00	0.14	4	0.35	−0.34	−0.02	−0.13
NGC 2552	0.0080	8.48	8.86	0.13	8.41	0.12	−0.16	0.30	4	0.15	−0.08	0.10	0.03	−0.03	0.03
NGC 3109	0.0040	8.48	9.06	0.00	8.77	0.00	0.02	0.05	1	0.15	−0.10	0.15	−0.02
NGC 3510	0.0080	0.00	9.73	0.31	8.72	0.21	−0.71	0.12	2	0.55	−0.52	0.14	0.02	−0.09	0.01

Notes.

^a A decay time of 0.00 denotes a constant SFR.

^b Model mass times 2, divided by model age. The model mass is corrected for the mass that has been returned to the ISM.

^c Number of models with the same fit rms out of seven models: constant SFR and six models with decaying SFRs.

^d Overall rms of the model fit to the colors.

^e Model color minus the observed integrated color of the galaxy.

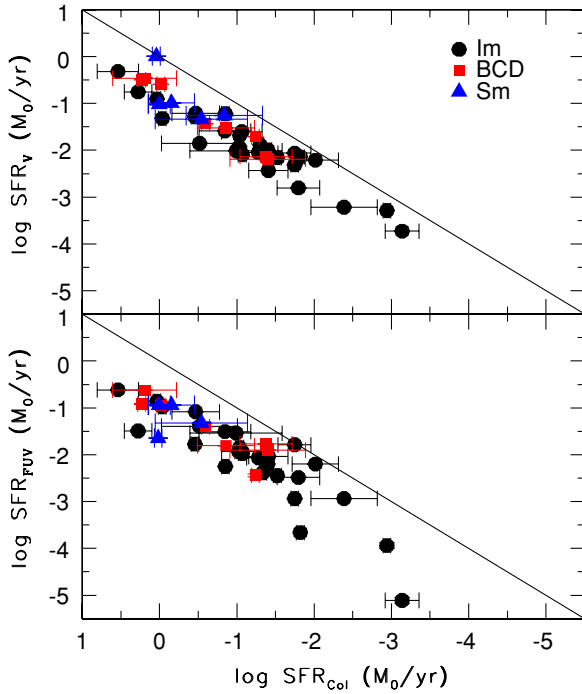


Figure 13. Star formation rate determined from population synthesis of integrated UV, optical, and near-IR colors SFR_{Col} plotted against SFRs determined from V-band and FUV luminosities. The solid line denotes equal SFRs. SFR_{Col} is greater than the other two SFR measures.

(A color version of this figure is available in the online journal.)

0.67 ± 0.25 . The similarity between this average observed value of $\log(\text{age}/t_d) = 0.67$ and the value required to give the observed $\text{SFR}_{\text{Col}}/\text{SFR}_{\text{FUV}} \sim 5$ is to be expected from the model.

Different star formation histories will produce slightly different offsets between the history-derived SFRs and the V-band or FUV-band SFRs. Star formation in small galaxies is likely to be bursty and gaspy, not steady or purely exponential as the models assume. Still, our main results should be robust: most dwarf irregulars had a period of more intense star formation in their 1 Gyr past than they do today, and this burst also exceeded the past average rate over the history of the galaxy. More finely tuned models should be able to find sub-bursts within this gigayear period. In our recent study of discrete star-forming regions in these same galaxies, we found factor of 2 variations in the SFRs on timescales ranging from 10's of millions of years to 1 Gyr using the age and mass distributions of the regions. The purpose of the present study is not to reproduce these bursty substructures in any detail using galaxy-wide colors, but only to illustrate the dominance of \sim Gyr-old star formation to the overall appearance of these galaxies. This gigayear dominance is not obvious at first when faced with the FUV images of 100 Myr old star formation and $\text{H}\alpha$ images of 10 Myr old star formation. The colors in fact suggest that these more recent events are relatively small compared to other events that typically occurred in the last gigayear.

6. RADIAL VARIATIONS FROM AZIMUTHALLY AVERAGED STAR FORMATION RATES

From the azimuthally averaged surface photometry, we calculate SFRs from the FUV, $\text{H}\alpha$, and V-band luminosities using the same prescriptions described in Section 5. However, here the SFRs are in units of $M_{\odot} \text{yr}^{-1} \text{kpc}^{-2}$ and correspond to elliptical

annuli of equal width and step size in increasing distance from the center of the galaxy. The ellipse parameters are given by Hunter & Elmegreen (2006). For a fourth SFR measure, we also modeled the colors of the annuli using the process described for the integrated photometry. For the annuli models, we assumed the best model type determined from the integrated SFR model, that is, constant star formation or decaying SFR. The model type is listed in Table 7 by decay timescale. The model fits to the observations were generally better for the annuli than for the integrated galaxy, so the χ^2 values were much lower. We therefore multiplied all of the color uncertainties by a factor of 5 instead of 20 in order to get non-zero Gaussian weights.

Radial profiles of all three of our luminosity-based SFR measures and the model SFR are plotted in Figures 14–16 as the ratio of SFR_{FUV} to $\text{SFR}_{\text{H}\alpha}$ (red curves), to SFR_{V} (blue curves) and to SFR_{Col} (green curves). The ratios for Im types in Figure 14 tend to be flat or falling with radius. The ratios for BCDs at the top of Figure 15 are mostly falling, and for Sm types at the bottom of Figure 15 are mostly flat. In addition, SFR_{Col} is always higher at each radius relative to SFR_{FUV} than are the other two SFR measures, consistent with the findings of Section 5.2.

The rising or falling trends in Figures 14–16 are quantified in the histogram given in Figure 17. Radial gradients in the logarithm of $\text{SFR}_{\text{FUV}}/\text{SFR}_{\text{H}\alpha}$ and the logarithm of $\text{SFR}_{\text{FUV}}/\text{SFR}_{\text{V}}$ were fit with a straight line, and in this figure we plot the number distribution of galaxies as a function of the slope of these gradients, normalized to the V-band disk scale length R_D^V . Some galaxy $\text{SFR}_{\text{FUV}}/\text{SFR}_{\text{V}}$ profiles were fit with two parts (nine dIm, four Sm), and in those cases the outer gradient is counted here. A flat radial distribution has a gradient of zero and is marked with a dashed vertical line in Figure 17. A positive gradient means that SFR_{FUV} becomes more dominant with radius than $\text{SFR}_{\text{H}\alpha}$ or SFR_{V} , and a negative gradient means that SFR_{FUV} becomes less dominant with radius. Figure 17 indicates that most of the galaxies have little or no gradient in $\text{SFR}_{\text{FUV}}/\text{SFR}_{\text{H}\alpha}$, meaning that the UV and $\text{H}\alpha$ -based SFRs on average track each other where both are measurable (i.e., where the $\text{H}\alpha$ and FUV coexist). However, $\text{SFR}_{\text{FUV}}/\text{SFR}_{\text{V}}$ gradients tend to be negative for the dIm and BCD types, while they are closer to zero for the Sm types.

The trends in Figures 14–17 follow from the other trends shown in this paper, and from the definitions of the various SFR indicators. BCDs have starbursts in their centers, so the SFR_{FUV} to SFR_{V} ratio tends to decrease with radius. The same is true for many Im galaxies, but not for the Sm's, which can have FUV spots relatively far out in their disks. The generally low values of $\text{SFR}_{\text{FUV}}/\text{SFR}_{\text{V}}$ most likely follow from higher past SFRs.

The similarity in radial gradients for SFR_{FUV} and $\text{SFR}_{\text{H}\alpha}$ shown on the right in Figure 17 suggests that the IMF is not getting steeper with radius over the radial range where both FUV and $\text{H}\alpha$ are observable. This is in agreement with the conclusions of Section 5.1.1.2 where we suggested that the missing $\text{H}\alpha$ in the outer regions is from faintness. It would be unlikely to see no difference in the two SFR gradients until there is a sudden lack of $\text{H}\alpha$ if the IMF were smoothly varying with surface brightness.

To see if there is any connection between the UV color gradient and the gradient in SFR, we plot Figure 18. The normalized $\log \text{SFR}_{\text{FUV}}/\text{SFR}_{\text{V}}$ gradient is plotted in Figure 18 along the x-axis, and the normalized FUV–NUV color gradient along the y-axis. High values on the y-axis indicate that the disk gets redder with increasing radius. The color profile, like the

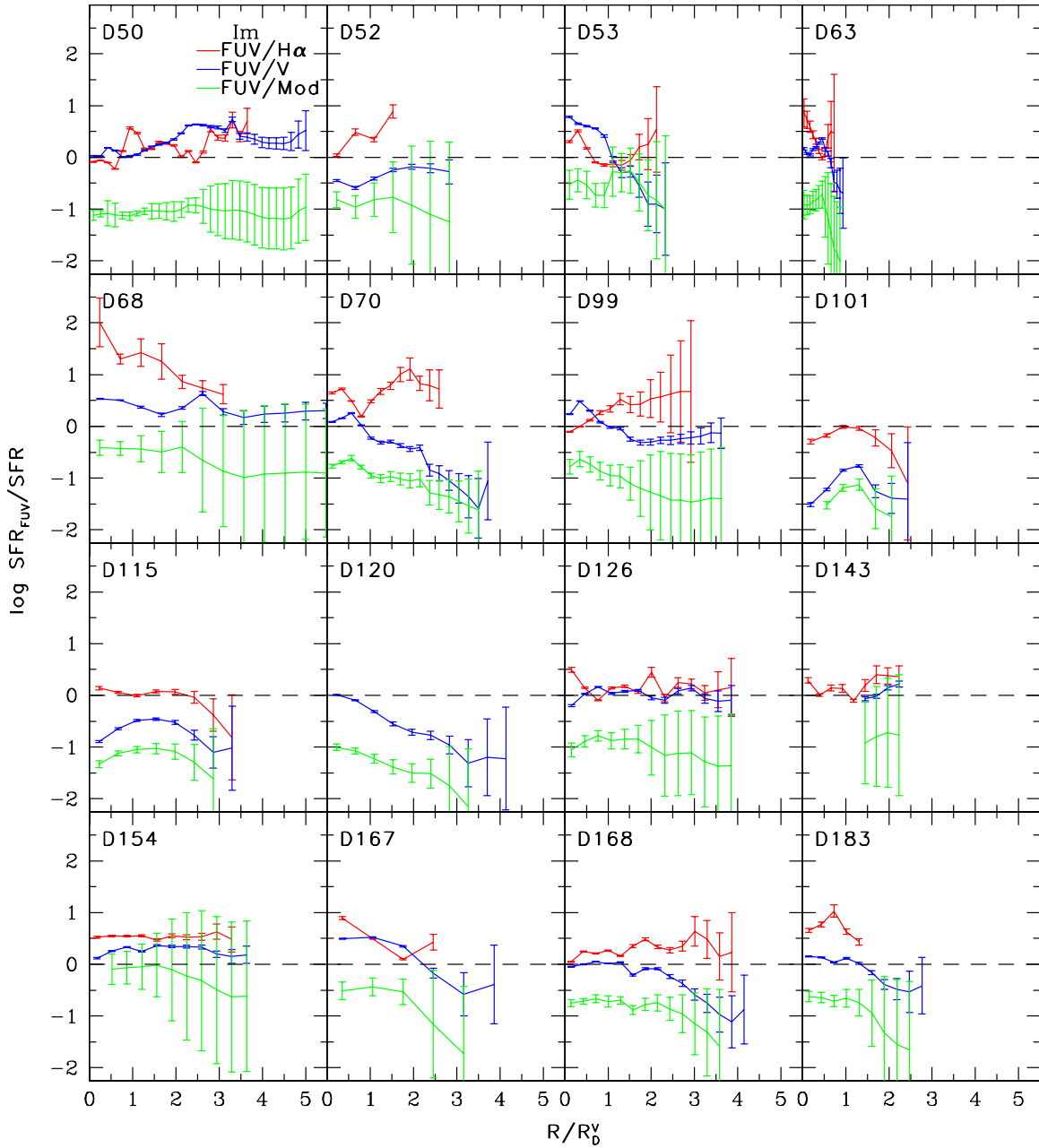


Figure 14. Azimuthally averaged SFRs determined from the FUV luminosity SFR_{FUV} divided by $\text{SFR}_{\text{H}\alpha}$ (red), by SFR_V (blue), and by SFR_{Col} (green) for the Im sample of galaxies. SFR_{Col} is a SFR determined from modeling the stellar populations and star formation histories from colors in annuli. SFR_V is determined from the mass in stars—calculated from M_V and a stellar M/L_V ratio that depends on $(B - V)_0$ —and assuming a constant SFR over 12 Gyr. The horizontal dashed lines mark equal SFRs, or ratios of 1. The ratios are plotted as a function of the radius normalized to the disk scale length measured from V surface brightness profiles R_D^V .

SFR ratio gradient, was sometimes fit with separate components for the inner and outer disks (five dImS, one BCD). For galaxies for which both quantities were fit with two components, the inner pair is plotted and the outer pair of values is plotted. For the cases where one quantity was fit with two components and the other was fit with one, both components of the two-part fit were plotted against the inner component of the single-part fit. Inner profile fits are denoted by filled symbols, and outer profiles are denoted by open symbols. The plotted points show a wide range of values. There are many galaxies with no color gradient but with a wide range in SFR ratio gradients. There are also galaxies with small gradients in the SFR ratio but prominent color gradients. Galaxies with gradients in both the SFR ratio

and UV color tend to show a wide range in color gradients for each SFR ratio gradient. Still, there is a trend in that galaxies with both gradients tend to get redder with radius and also have decreasing SFR_{FUV} relative to SFR_V with increasing radius. These trends suggest that *sometimes* star formation stops in the outer disk for a relatively long time.

One possible reason for outer disk truncation in star formation is the lack of gas. We do not yet have H I maps of these galaxies, so we cannot make a definitive statement on this issue. However, we do have total H I masses, and these are plotted in Figure 19. The abscissa has the log of the ratio of total H I mass to B -band luminosity, and the ordinate has the normalized SFR-ratio gradient in the bottom panel and

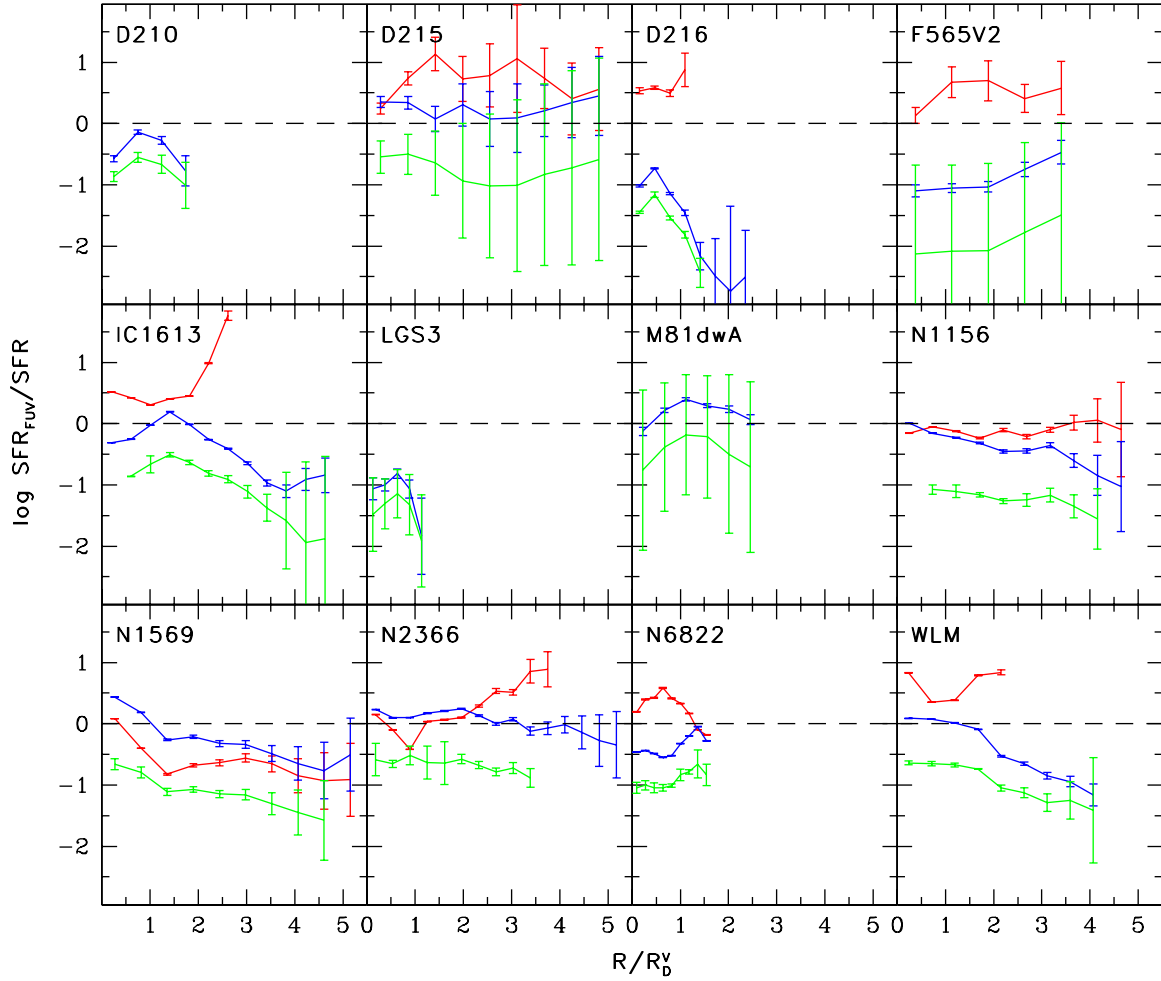


Figure 14. (Continued)

the normalized UV color gradient in the top panel. In this case, the SFR-ratio gradient is that only for the outer disk, if fit with two parts. Evidently, low M_{HI}/L_B does correspond to both an outer disk reddening and an outer disk drop in SFR_{FUV} relative to disk mass. These cases presumably have halted outer disk star formation because of a lack of outer disk gas. Above $\log M_{\text{HI}}/L_B \sim -0.5$, however, this correlation disappears. Galaxies with relatively high HI mass can have either large or small SFR-ratio gradients, although most of them have small UV color gradients. Such variations in SFR-ratio gradient should correlate with color gradients if the SFR gradients in the disk are long term. Recall that $\text{SFR}_{\text{H}\alpha}$ measures star formation in the last few tens of megayears, $\text{FUV} - \text{NUV}$ measures star formation in the last hundred megayears or so, and SFR_V measures the average SFR over a Hubble time. Thus, a more likely explanation for the behavior of $\text{SFR}_{\text{FUV}}/\text{SFR}_V$ and $\text{FUV} - \text{NUV}$ at high M_{HI}/L_B is a short time variation in the outer disk SFR. Observations that are sensitive to the timescale for variations, such as SFR_{FUV} , will mimic those variations and show a lot of scatter, while observations that are sensitive only to longer-term variations, such as $\text{FUV} - \text{NUV}$ or SFR_V , will average over the short-term effects and show only a constant or slowly varying rate. Thus, we suggest that galaxies with low M_{HI}/L_B have essentially stopped their star formation in the outer disk, while galaxies with intermediate and high M_{HI}/L_B have variable star formation in the outer disk

with a timescale of several tens of millions to a hundred million years.

In Figure 20, we plot the slope of the normalized gradient in $\log \text{SFR}_{\text{FUV}}/\text{SFR}_V$ against galactic M_V . There is a rough correlation in the sense that galaxies with more negative gradients are fainter. We do not find an equally clear correlation between $\text{FUV} - \text{NUV}$ color gradient and M_V (although there is the usual correlation between M_{HI}/L_B and M_V in the sense that smaller galaxies have relatively more HI). Figure 20 is consistent with a model in which small galaxies have more time fluctuations in the SFR.

We note that observations that are sensitive to a certain time interval for star formation will show fluctuations only over the radial range in a galaxy where the variability has a comparable timescale. Generally, the density of interstellar gas decreases with radius and the timescale for SFR variations increases. Thus, observations like FUV that are sensitive to ~ 100 Myr old stellar populations will show the strongest fluctuations in the outer disk, where the dynamical timescale is larger than this.

7. DISCUSSION

7.1. Results

Observations at FUV, NUV, V, and $\text{H}\alpha$ of integrated magnitudes, radial profiles, and SFRs for dIm, BCD, and Sm galaxies reveal star formation in outer disks that is a smooth continuation

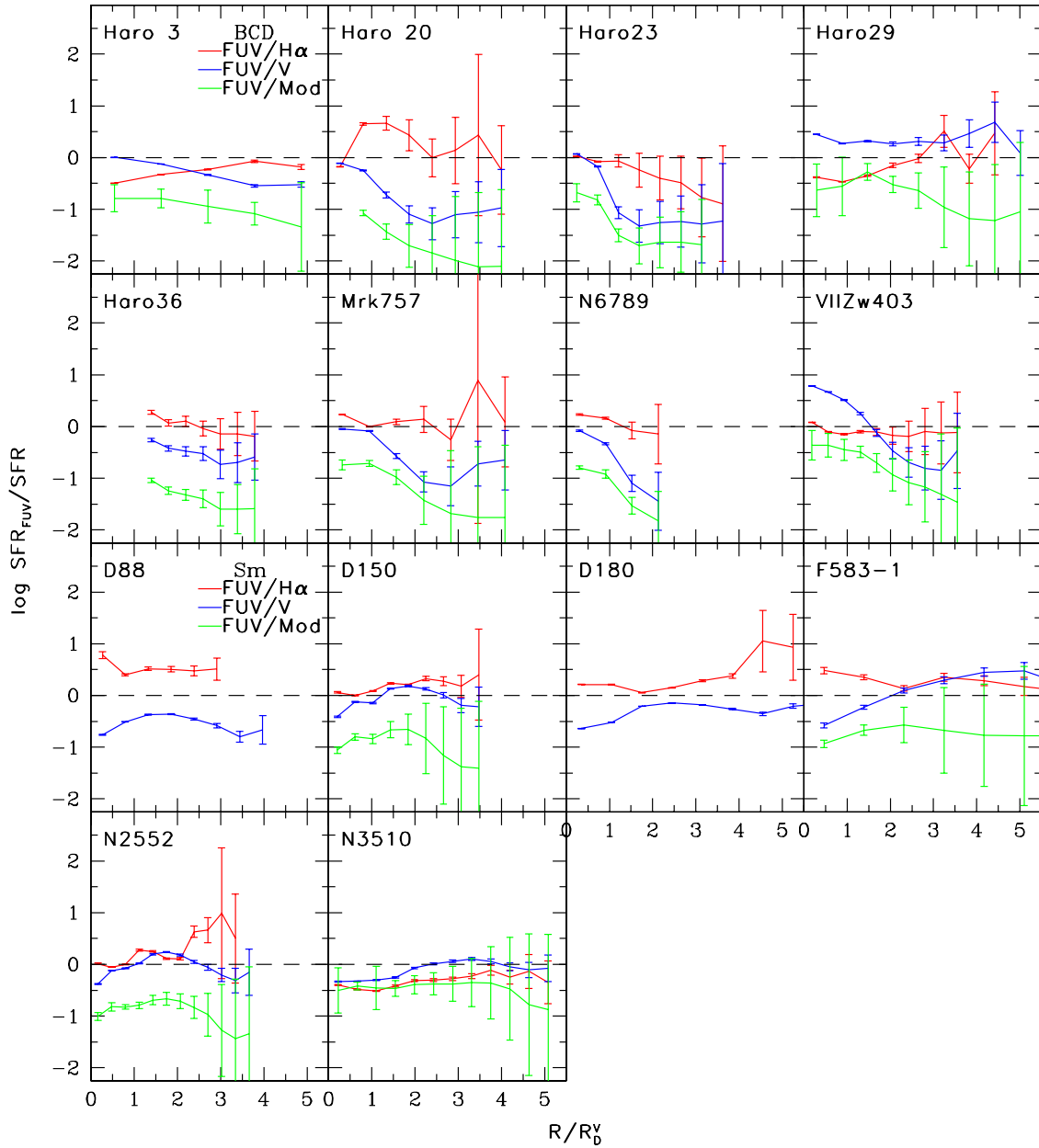


Figure 15. Ratios of azimuthally averaged SFRs (SFRs) vs. normalized radius, as in Figure 14, for the BCD (top two panels) and Sm (bottom two panels) samples of galaxies. The BCDs tend to have decreasing ratios with increasing radius, and the SmS tend to have flat or increasing ratios.

of the inner disk activity, with a bursty nature on a timescale of ~ 1 Gyr. Surface brightness levels are observed down to ~ 29 mag arcsec $^{-2}$ in NUV and ~ 27 mag arcsec $^{-2}$ in V (Figure 4). The $(FUV - NUV)_0$ and $(NUV - V)_0$ colors are usually red in the outer disk, and often increasingly red with galactocentric radius, indicating a slowdown of star formation in the outer parts over the last gigayear. The BCD and Im galaxies, which are physically small ($R_D^V \sim 0.2$ – 1 kpc), tend to be the ones with red outer disks, and they have V-band scale lengths larger than those measured in the NUV band by a factor of ~ 1.2 (Figure 5). The Sm galaxies, which can be physically large ($R_D^V \sim 0.5$ – 3 kpc), tend to have blue outer disks and V-band scale lengths that are smaller than those measured in the NUV band.

These color trends are reproduced by trends in star formation indicators. Short-term indicators like H α behave differently with radius than intermediate and long-term indicators like FUV and V band, respectively. Galaxies that get redder with radius tend to

have radially decreasing FUV relative to V SFRs, while galaxies that get bluer with radius tend to have radially increasing FUV relative to V star formation. The smallest integrated SFRs are on the order of 10^{-3} – $10^{-4} M_\odot \text{ yr}^{-1}$. The smallest areal SFRs are on the order of 10^{-4} – $10^{-5} M_\odot \text{ yr}^{-1} \text{ kpc}^{-2}$ (Figure 8), as measured by H α . At these rates, the surface density of stars formed after a Hubble time is only $\sim 1 M_\odot \text{ pc}^{-2}$ on average inside a $\sim 4 \text{ kpc}^2$ disk, the typical size for our galaxies. The stellar surface densities are much lower in the outer parts. We return to this point below.

Double exponential disks, with steeper or shallower outer parts than inner parts, are observed in this sample (Figure 4). Usually, the NUV follows the V band, where double exponentials were already observed (Hunter & Elmegreen 2006). There is often no obvious $(FUV - NUV)_0$ color change at the break radius (e.g., DDO 68, DDO 75, F565V2, DDO 150), although sometimes there is (DDO 101, DDO 183, M81dwa), and

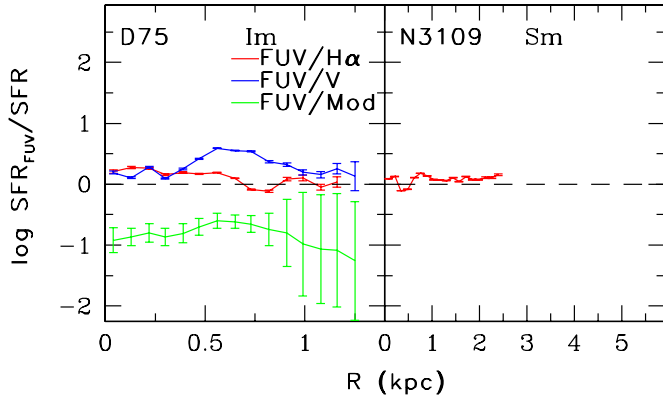


Figure 16. Ratios of azimuthally averaged SFRs, as in Figure 14, vs. radius in kpc for two galaxies without R_D^V measures. The galaxy on the left is an Im system and the one on the right is an Sm.

sometimes there is an abrupt color change without a break in the radial profile (e.g., IC 1613). This ambiguity in color breaks, in addition to the lack of spiral density waves in our sample, suggests that the outer exponential is not the result of spiral wave-scattered stars, as proposed for spiral galaxies by Roskar et al. (2008). No disk terminations have been observed in our sample, even down to the faintest levels and largest radii obtained, which is usually with the V and NUV observations.

Generally, the outer disks of galaxies typically lack H α emission even though there is star formation at some level seen in the FUV. The same is true for our sample. We find a smooth correlation between the ratio of FUV to H α SFRs versus the absolute SFR, of the form $\text{SFR}_{\text{FUV}}/\text{SFR}_{\text{H}\alpha} \propto \text{SFR}_{\text{H}\alpha}^{-0.59 \pm 0.07}$.

This is essentially the same correlation as that found by Meurer et al. (2009) for different galaxies. We disagree with the conclusions in Meurer et al., however. They considered this correlation to be the result of a steepening stellar IMF with galactocentric radius, so that outer disk star formation lacks O-type stars and the associated ionization compared to inner disk star formation. However, pervasive FUV in the outer disks and the radially invariant FUV – V colors in many cases suggest that the IMF does not change with radius and the missing H α is from a lack of gas, i.e., from density-bounded H II regions in the classical sense. At the very least, this says that the stars that produce the FUV – V colors are not varying, but the range of masses responsible for H α emission could be. At very low ambient densities, this H II region limitation, which is usually in reference to local conditions near giant molecular clouds, translates into a limit for the whole thickness of the local disk (“saturated ionization”). We showed in Section 5.1.1 that for constant disk thickness over the radial range where H α is observed, and for a local SFR proportional to n_{gas}^γ , the observed ratio becomes $\text{SFR}_{\text{FUV}}/\text{SFR}_{\text{H}\alpha} \propto \text{SFR}_{\text{H}\alpha}^{\gamma/2-1}$. Typically, $\gamma \sim 1-1.5$, and the observed slope of this correlation is reproduced. Beyond the radial range where H α is observed, the disk thickness probably flares, making the ionization even more diffuse and any associated H α even harder to observe. Thus, we believe H α is lacking because the gas density is too low to show the associated emission measure. We predict that more sensitive observations of H α or other ionization tracers over large regions around each star formation site will show the presence of ionization.

Models for the color profiles of our galaxies considered an exponentially decaying star formation history with a constant

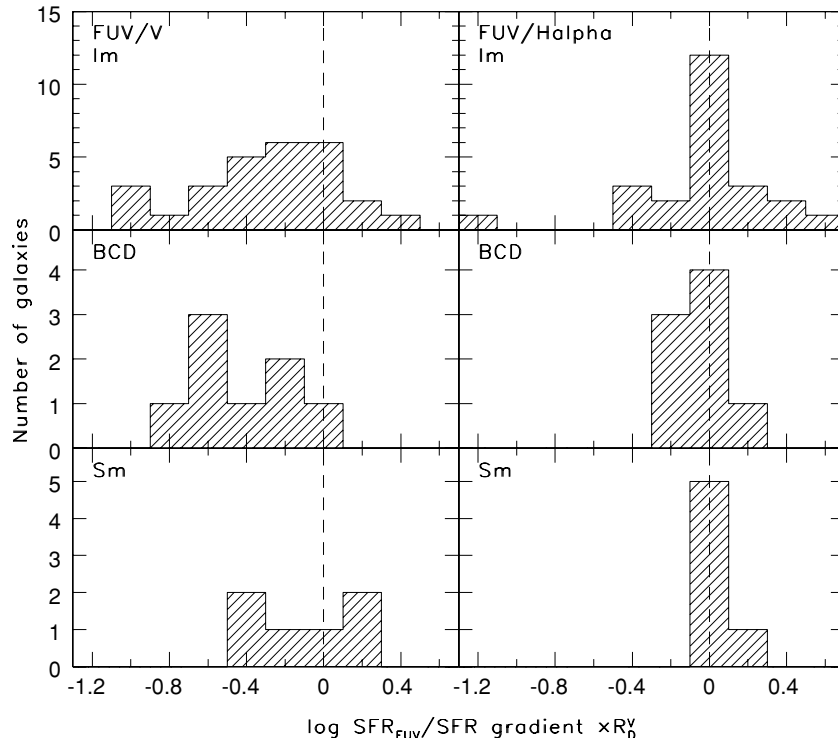


Figure 17. Number of galaxies as a function of normalized SFR gradient: $\text{SFR}_{\text{FUV}}/\text{SFR}_{\text{H}\alpha}$ (right) and $\text{SFR}_{\text{FUV}}/\text{SFR}_V$ (left). Some of the galaxy $\text{SFR}_{\text{FUV}}/\text{SFR}_V$ profiles were fit with two parts. In those cases the outer gradient is counted here. A flat radial distribution has a gradient of zero and that value is marked with a dashed vertical line. A positive gradient means that SFR_{FUV} becomes more dominant with radius; a negative gradient means that $\text{SFR}_{\text{H}\alpha}$ or SFR_V becomes more dominant with radius compared to the UV.

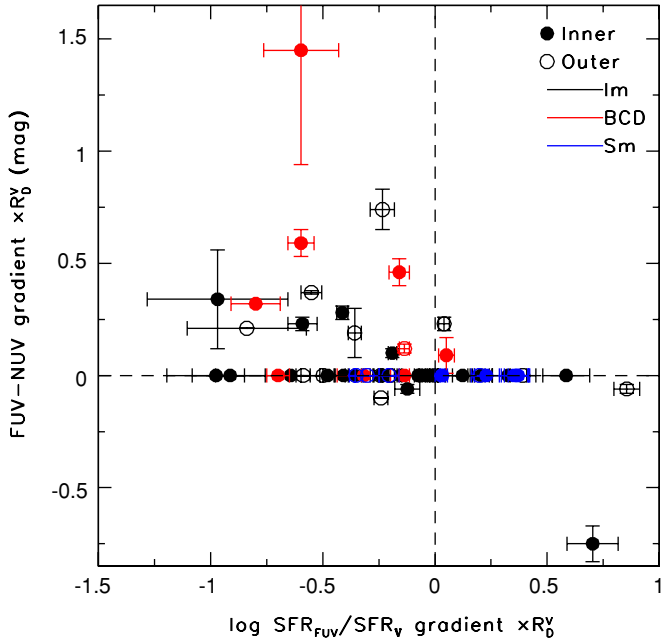


Figure 18. Gradient in $(FUV - NUV)_0$ vs. gradient in $\log SFR_{FUV}/SFR_V$. Both gradients have been normalized to the V -band disk scale length R_D^V . The UV color gradient and SFR_{FUV}/SFR_V profiles, in some cases, were fit with two components. For galaxies for which both quantities were fit with two components, the inner pair is plotted and the outer pair of values is plotted. For the cases where one quantity was fit with two components and the other was fit with one, both components of the two-part fit were plotted against the single-part fit in the other quantity. We see that those galaxies that do show gradients in both the SFR ratio and UV color tend to show a range in color gradients for similar SFR ratio gradients. Most color gradients are toward redder $(FUV - NUV)_0$ at larger radius and toward lower SFR_{FUV} relative to SFR_V at larger radius.

IMF. The resulting average SFRs were compared to the $H\alpha$, FUV, and V -band rates. There is a general agreement between all of these rates if the SFRs were higher in the past and the star formation ages or burst ages in the outer disks are ~ 1 Gyr or a few gigayears. A higher rate in the past also helps us to explain how the FUV profiles can be steeper than the V -band profiles, especially in Im galaxies (Figure 4). Current star formation following steep FUV profiles cannot continue building a disk with the same mass distribution indicated by the shallow V -band profiles. The disk scale lengths will get smaller over time if the FUV profiles alone reflect a long future of star formation. Outer disk bursts with \sim Gyr timescales mitigate this problem, allowing the disks to build up in a self-similar although chaotic way, or even with increasing disk scale lengths over time. The Sm galaxies with relatively blue outer disks and high outer disk SFRs could be examples of outer disk building. Perhaps the morphology changes from Im to Sm during this outer active phase, because the Sm types have more extended and bluer outer disks compared to the Im types.

There is a correlation between the outward red $FUV - V$ gradients and the $H I$ mass-to-light ratio of the galaxy in the sense that galaxies with the lowest relative $H I$ mass have the largest scale-normalized gradients in the ratios of FUV to V -band SFRs (Figure 19). We interpret this to imply that some outer disks are red because star formation virtually stops there with a lack of gas. Galaxies with intermediate to high relative $H I$ masses have a wide range of gradients in the SFR ratio, which implies that outer disk star formation is ongoing, but bursty, as indicated by our other results.

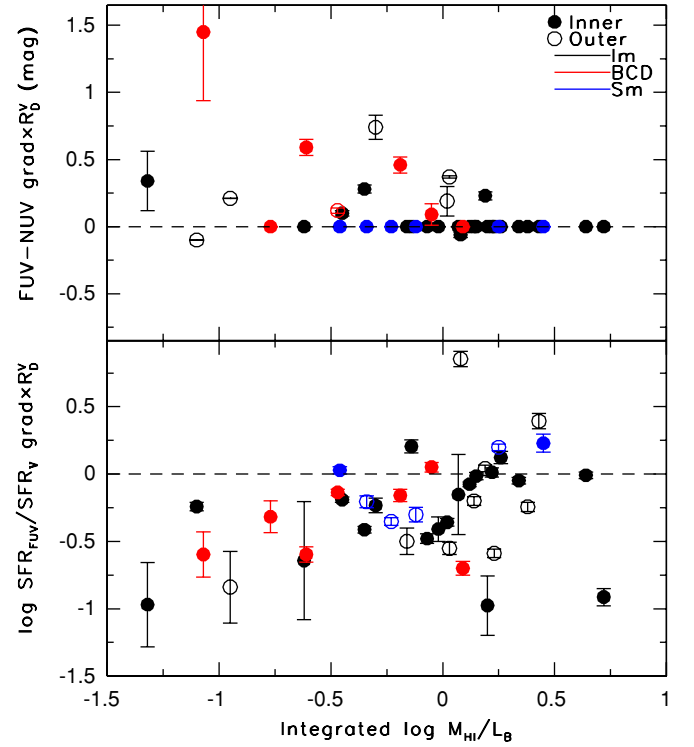


Figure 19. Galactic integrated $H I$ mass to L_B ratio plotted against the gradient in $(FUV - NUV)_0$ (top) and $\log SFR_{FUV}/SFR_V$ (bottom). Both gradients have been normalized to the V -band disk scale length R_D^V . The horizontal dashed lines mark gradients of zero. For profiles fit with two lines, both the inner and outer gradients are plotted.

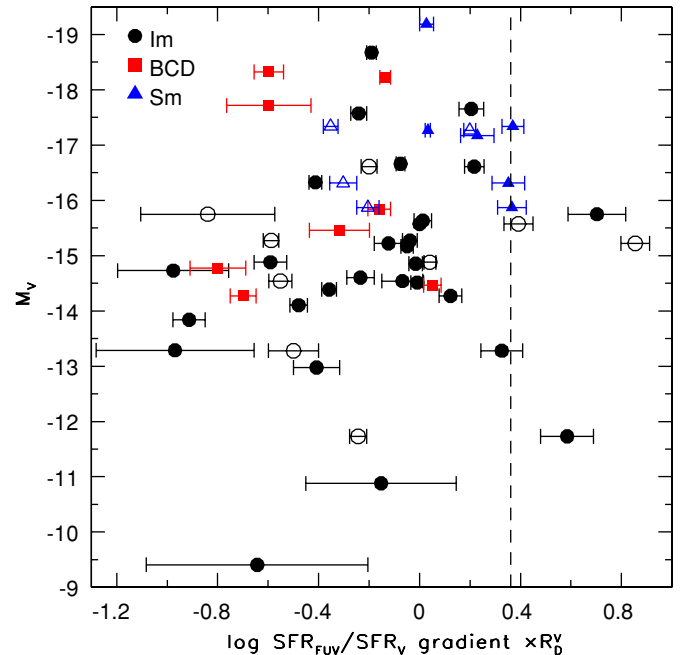


Figure 20. Gradient in $\log SFR_{FUV}/SFR_V$ normalized to the V -band disk scale length R_D^V vs. galactic M_V . Filled symbols are for inner SFR_{FUV}/SFR_V gradients and open symbols are for outer SFR_{FUV}/SFR_V gradients for those profiles that were fit with two lines.

Perhaps the most remarkable result of this survey is the low level of FUV emission in the far-outer disks of late-type and dwarf irregular galaxies. Star formation is apparently continuing

there at an extremely low level. In the following subsection, we model the population and surface density in the far outer parts of the disks, and consider the implications of these models for star formation and galaxy buildup.

7.2. Models for Far Outer Disk Colors and Surface Brightnesses

Figure 4 summarizes most of the key observations in our study and indicates several main features of outer disks. First the FUV – V colors are usually in the range of ~ 1 – 3 mag, which are typical of star-forming galaxies (Wyder et al. 2007). Nevertheless, the surface brightness level in the FUV also gets very low, down to ~ 29 mag arcsec $^{-2}$ in some cases, with no indication of a turnover. In V band, the surface brightness may reach ~ 26 to ~ 28 mag before it gets too faint to see. These colors and surface brightnesses place interesting constraints on the stellar populations and surface densities in the outer disk.

We consider again the models of Bruzual & Charlot (2003) for the Salpeter IMF at two metallicities, 0.4 solar and 0.2 solar. Figure 21 shows the absolute magnitudes at 2267 Å, the effective wavelength of the NUV filter, and V for a single stellar population (SSP) model starting with $1 M_{\odot}$ of stars (red and blue curves). The populations get fainter as they age, with the FUV getting faint faster than the V band; the cross over occurs at an age of $\sim 10^{7.4}$ yr. The black curves are the 2267 – V colors for a constant SFR; this model also gets redder with age, but much slower than the SSP model: only after $10^{8.2}$ yr does the 2267 – V color become positive and it never gets much above 1, unlike the observations in Figure 4. Thus, the observation of red colors in the outer disks of our sample, along with the observation of steeper FUV profiles than V profiles, supports the SSP model more than the constant SFR model. That is, star formation is bursty, particularly in the outer disks, with an off time comparable to or larger than 1 Gyr, which is what it takes to make 2267 – V positive.

Figure 22 shows the surface density of stars versus age in the SSP (blue, red, magenta curves) and constant SFR models (black curves) for a surface brightness in the FUV of ~ 29 mag arcsec $^{-2}$ (blue curves) and two sample surface brightnesses in the V band, ~ 28 mag arcsec $^{-2}$ (red), and ~ 29 mag arcsec $^{-2}$ (magenta). A green square outlines the intersection point where FUV and V surface brightnesses give the same mass surface density, as required for a sensible model. The models with a constant SFR are generally too blue to produce a sensible model: the $M_{2267} = 29$ mag arcsec $^{-2}$ black curve never intersects the $M_V = 27$ mag arcsec $^{-2}$ black curve and it only intersects the $M_V = 28$ mag arcsec $^{-2}$ black curve at a very late time, $10^{9.4}$ yr. The results suggest that the age of the stellar population in a typical outer disk is several hundred megayears, without much star formation in the intervening time. This is consistent with the ages obtained from other observations and models in this paper. Also, the surface density in the outer disk is $\sim 0.1 M_{\odot}$ pc $^{-2}$. This is the lowest surface density that we measure here, corresponding to the faintest FUV surface brightness. Presumably, surface density goes even lower at larger radii.

A surface density of $\sim 0.1 M_{\odot}$ pc $^{-2}$ corresponds to a gas column density of $\sim 10^{19}$ cm $^{-2}$, which also corresponds to 0.01 mag of extinction at solar abundances. This is extremely low compared to the main disks of spiral galaxies. For example, the stellar surface density near the Sun is $\sim 70 M_{\odot}$ pc $^{-2}$. It is much lower than the canonical gas threshold for star formation of several M_{\odot} pc $^{-2}$. However, the outer disks of our galaxies are gas dominated, with gas surface densities larger than stellar

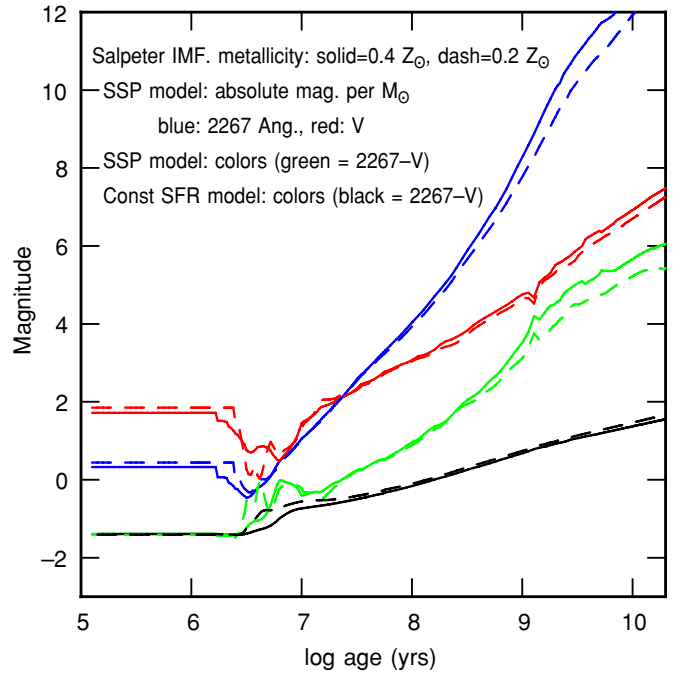


Figure 21. Models from Bruzual & Charlot (2003) of the evolution of absolute magnitude for a single population of $1 M_{\odot}$ of stars at 2267 Å and V band (blue and red lines, respectively). Green curves show the 2267 – V colors in that model. The black curves are for a constant SFR. Because the observations suggest red 2267 – V colors of 1–3 mag in the outer parts of our sample disks, only the SSP models with star formation ending ~ 100 Myr ago or longer are acceptable. Two metallicities are represented by different line types. *GALEX* magnitudes in the rest of this paper are on the AB scale, and V magnitudes are on the Vega scale. Bruzual & Charlot (2003) magnitudes are also on the Vega scale. To make the color NUV – V in this figure have the same meaning as in the rest of this paper, we added 1.8 to the Bruzual & Charlot NUV magnitudes to put them on the AB scale. This correction comes from the Vega flux (Castelli & Kurucz 1994) for the effective wavelength of the NUV filter, 2267 Å.

by factors of ~ 2 – 5 or even 10 beyond several times R_D^V (D. Hunter 2009, private communication). This is still below the conventional star formation threshold for gas (see also Melena et al. 2009), but evidently not without the ability to form stars.

A stellar surface density of $\sim 0.1 M_{\odot}$ pc $^{-2}$ also corresponds to an average SFR of $\sim 10^{-4} M_{\odot}$ yr $^{-1}$ kpc $^{-2}$ over a gigayear, which is comparable to the low end of the SFRs we have measured here for outer disks. It would be 10 times lower on average if the age were a Hubble time. For a typical galaxy rotation speed of ~ 100 km s $^{-1}$ and a typical outer radius of ~ 2.5 kpc (Figure 4), the rotation period is ~ 160 Myr, so there were ~ 6 rotations as these stars formed in the last gigayear. Also, in a kpc wide band at 2.5 kpc radius, there is an area of 15.7 kpc 2 , so the average SFR in this band over the last gigayear is $\sim 10^{-3} M_{\odot}$ yr $^{-1}$. Considering a normal IMF, where it takes $10^3 M_{\odot}$ of stars overall to form a single $\sim 60 M_{\odot}$ O-type star (for a Salpeter power-law slope at intermediate to high mass and a turnover below $0.5 M_{\odot}$), it appears that the outer one-third of the disks of our galaxies have formed an average of about one O-type star per million years. There should, therefore, be only a few such massive stars at any one time even if the SFR were constant. In fact there should be far fewer in the cases studied here where star formation appears to have ended ~ 1 Gyr ago. A lack of O-type stars from statistically sampling a normal IMF at very low SFRs could also reduce the H α flux below expectations.

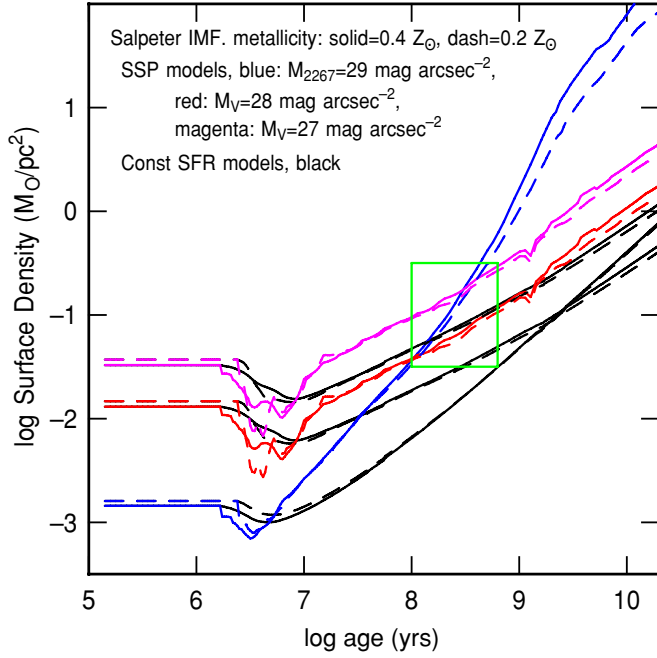


Figure 22. Mass surface density is shown vs. population age for a surface brightness at 2267 Å of 29 mag arcsec⁻² (blue curves) and surface brightnesses at V-band of 27 and 28 mag arcsec⁻² (magenta and red, respectively). The 2267 Å and V-band curves intersect at the most likely value for the observations, which is indicated by the green box. This result suggests that the outer disk has an age of several hundred megayears and a surface density of $\sim 0.1 M_{\odot} \text{pc}^{-2}$. The black lines are for a constant SFR, which does not give a solution (i.e., the same surface density fit for both passbands) in a reasonable age. Two metallicities are represented by different line types.

8. CONCLUSIONS

We have presented UV-integrated and azimuthally averaged surface photometric properties of a sample of 44 dIm, BCD, and Sm galaxies. The UV measurements come from analysis of archival NUV and FUV images obtained with *GALEX*, and we compare the UV to H α and V-band properties. We convert FUV, H α , and V-band luminosities into SFRs. We also fit model stellar populations to colors for an alternate SFR measure for seven different assumed star formation histories. We compare integrated SFRs and SFR profiles with radius in these four measures.

In most of the galaxies, the measures of SFRs track each other with radius. However, the UV profile often extends further in radius than the H α profile, providing a better measure of the star formation activity in outer disks. Most of the dIm galaxies have constant or slightly increasing UV color with radius, as do the BCDs, while the Sm galaxies, which are also larger than the others, sometimes get bluer with radius. Star formation often extends so far into the outer disk that it would appear to be sub-threshold, according to conventional ideas. Such star formation may result from local triggering or from gravitational instabilities with angular momentum removal during cloud formation (Melena et al. 2009).

We find that integrated SFRs determined from H α are lower than SFRs determined from FUV for all but the highest SFR systems. The discrepancies are unlikely due to underestimated extinction, plausible alternative conversion factors, or a larger contribution from older stars where the SFR is lower. On the other hand, the SFR determined from M_V is the same on average as the FUV-based SFR for all but the lowest SFR systems, but with a large scatter about the equivalency relationship. This is

consistent with a generally constant SFR that varies by factors of a few over long times. In addition, the SFR determined from modeling colors is always higher than the other three SFR measures, perhaps because the SFR has decayed over time, although it almost always has the same radial profile shape as SFR_V.

Galaxies with the largest discrepancies between FUV-observed SFRs and V-band observed SFRs also have the lowest relative H I masses. We suggest that the outer disks of these galaxies have very low gas column densities, causing a cessation in star formation, while in galaxies with relatively high H I masses, the star formation in the outer disk can be active or not with fluctuations on a gigayear timescale.

The lack of H α in the outer disk is most likely the result of faint emission measures, rather than the result of radially varying or peculiar IMFs. This conclusion follows quantitatively from a correlation between the ratio of SFRs in FUV and H α and the absolute H α SFR. In our interpretation, a significant amount of H α flux is missing from the outer disk star-forming regions, and so the SFR determined from H α is too low. We fit the observed correlation to a model with a constant disk thickness and a density-dependent star formation law.

The stellar surface densities in the outer parts of our galaxies reach values as low as $\sim 0.1 M_{\odot} \text{pc}^{-2}$, and the SFRs get as low as $\sim 10^{-4} M_{\odot} \text{yr}^{-1} \text{kpc}^{-2}$ for gigayear periods. Most likely the star formation in these regions is sub-threshold in the conventional sense. There is no evident break in the FUV radial profiles from the inner disks that might correspond to a star formation threshold, aside from the occasional presence of a kink in the exponential disk that seems unrelated to color changes. The kink is often far inside the furthest measured radius anyway, and thus apparently unrelated to a physical disk edge. No such edges have been observed yet.

B.C.L. participated in the 2006 Research Experience for Undergraduates (REU) program at Northern Arizona University (NAU). We appreciate Kathy Eastwood's efforts in organizing that program and the National Science Foundation for funding it through grant AST-0453611 to NAU. Funding for this research was provided to D.A.H. and B.G.E. by NASA-GALEX grant NNX07AJ36G and by cost-sharing from the Lowell Observatory. This research has made use of the NASA/IPAC Extragalactic Database (NED) which is operated by the Jet Propulsion Laboratory, California Institute of Technology, under contract with the National Aeronautics and Space Administration. We also appreciate constructive suggestions from an anonymous referee.

Facilities: GALEX, Lowell Observatory

REFERENCES

- Alongi, M., Bertelli, G., Bressan, A., Chiosi, C., Fagotto, F., Greggio, L., & Nasi, E. 1993, *A&AS*, **97**, 851
- Bell, E. F., & Bower, R. G. 2000, *MNRAS*, **319**, 235
- Bell, E. F., & de Jong, R. S. 2001, *ApJ*, **550**, 212
- Boissier, S., et al. 2007, *ApJS*, **173**, 524
- Boissier, S., et al. 2008, *ApJ*, **681**, 244
- Bressan, A., Fagotto, F., Bertelli, G., & Chiosi, C. 1993, *A&AS*, **100**, 647
- Brinchmann, J., Charlot, S., White, S. D. M., Tremonti, C., Kauffmann, G., Heckman, T., & Brinkmann, J. 2004, *MNRAS*, **351**, 1151
- Bruzual, G., & Charlot, S. 2003, *MNRAS*, **344**, 1000
- Buat, V., et al. 2005, *ApJ*, **619**, L51
- Burstein, D., & Heiles, C. 1984, *ApJS*, **54**, 33
- Cairós, L. M., Vilchez, J. M., González Pérez, J. N., Iglesias-Páramo, J., & Caon, N. 2001, *ApJS*, **133**, 321
- Cardelli, J. A., Clayton, G. C., & Mathis, J. S. 1989, *ApJ*, **345**, 245

- Castelli, F., & Kurucz, R. L. 1994, *A&A*, **281**, 817
- Corbelli, E., Verley, S., Elmegreen, B. G., & Giovanardi, C. 2009, *A&A*, **495**, 479
- Elias, F., Alfaro, E. J., & Cabrera-Caño, J. 2009, *MNRAS*, **397**, 2
- Elmegreen, B. G. 2004, *MNRAS*, **354**, 367
- Elmegreen, B. G. 2006, *ApJ*, **648**, 572
- Elmegreen, B. G. 2008, *ApJ*, **672**, 1006
- Elmegreen, B. G., & Hunter, D. A. 2006, *ApJ*, **636**, 712
- Fagotto, F., Bressan, A., Bertelli, G., & Chiosi, C. 1994a, *A&AS*, **104**, 365
- Fagotto, F., Bressan, A., Bertelli, G., & Chiosi, C. 1994b, *A&AS*, **105**, 29
- Galliano, F., et al. 2003, *A&A*, **407**, 159
- Gordon, K. D., & Clayton, G. C. 1998, *ApJ*, **500**, 816
- Gordon, K. D., Clayton, G. C., Misselt, K. A., Landolt, A. U., & Wolff, J. J. 2003, *ApJ*, **594**, 279
- Hirashita, H., Buat, V., & Inoue, A. K. 2003, *A&A*, **410**, 83
- Hunter, D. A., & Elmegreen, B. G. 2004, *ApJ*, **128**, 2170
- Hunter, D. A., & Elmegreen, B. G. 2006, *ApJS*, **162**, 49
- Hunter, D. A., Elmegreen, B. G., & Baker, A. L. 1998, *ApJ*, **493**, 595
- Hunter, D. A., Elmegreen, B. G., & Martin, E. 2006, *ApJ*, **132**, 801
- Hunter, D. A., & Hoffman, L. 1999, *ApJ*, **117**, 2789
- Hunter, D. A., & Plummer, J. D. 1996, *ApJ*, **462**, 732
- Iglesias-Páramo, J., et al. 2006, *ApJS*, **164**, 38
- Kennicutt, R. C., Jr. 1998, *ARA&A*, **36**, 189
- Leitherer, C., et al. 1999, *ApJS*, **123**, 3
- Leroy, A. K., Walter, F., Brinks, E., Bigiel, F., de Blok, W. J. G., Madore, B., & Thornley, M. D. 2008, *ApJ*, **136**, 2782
- Marconi, G., Tosi, M., Greggio, L., & Focardi, P. 1995, *ApJ*, **109**, 173
- Martin, D. C., et al. 2005, *ApJ*, **619**, L1
- Melena, N. W., Elmegreen, B. G., Hunter, D. A., & Zernow, L. 2009, *ApJ*, **138**, 1203
- Meurer, G. R., Carignan, C., Beaulieu, S. F., & Freeman, K. C. 1996, *ApJ*, **111**, 1551
- Meurer, G. R., et al. 2009, *ApJ*, **695**, 765
- Noeske, K. G., Papaderos, P., Cairós, L. M., & Fricke, K. J. 2003, *A&A*, **410**, 481
- Papaderos, P., Loose, H.-H., Fricke, K. J., & Thuan, T. X. 1996, *A&A*, **314**, 59
- Pflamm-Altenburg, J., Weidner, C., & Kroupa, P. 2007, *ApJ*, **671**, 1550
- Rafikov, R. R. 2001, *MNRAS*, **323**, 445
- Richer, M. G., & McCall, M. L. 1995, *ApJ*, **445**, 642
- Roskar, R., Debattista, V. P., Stinson, G. S., Quinn, T. R., Kaufmann, T., & Wadsley, J. 2008, *ApJ*, **675**, 65
- Salim, S., et al. 2007, *ApJS*, **173**, 267
- Salpeter, E. E. 1955, *ApJ*, **121**, 161
- Thilker, D. A., et al. 2005, *ApJ*, **619**, L79
- Thilker, D. A., et al. 2007a, *ApJS*, **173**, 538
- Thilker, D. A., et al. 2007b, *ApJS*, **173**, 572
- Treyer, M., et al. 2007, *ApJS*, **173**, 256
- van Zee, L., Haynes, M. P., Salzer, J. J., & Broeils, A. H. 1997, *ApJ*, **113**, 1618
- Whitmore, B. C. 2003, in *A Decade of HST Science*, ed. M. Livio, K. Noll, & M. Stiavelli (Cambridge: Cambridge Univ. Press), 153
- Wong, T., & Blitz, L. 2002, *ApJ*, **569**, 157
- Wyder, T. K., et al. 2007, *ApJS*, **173**, 293